Fulleride superconductivity tuned by elastic strain due to cation compositional disorder

H. Esma Okur,[a] Ross H. Colman,[b] Yasuhiro Takabayashi,[c] Peter Jeglič,[d] Yasuo Ohishi,[e] Kenichi Kato,[f] Denis Arčon,[d,g] Yoshiki Kubota,[h] and Kosmas Prassides*[d,h,i]

[a.] *Department of Chemistry, Faculty of Engineering and Natural Sciences, Bursa Technical University, TR-16310 Bursa, Turkey*

[b.] *Department of Condensed Matter Physics, Faculty of Mathematics and Physics, Charles University, 121 16 Prague, Czech Republic*

[c.] *Department of Physical Science and Engineering, Nagoya Institute of Technology, Nagoya 466-8555, Japan*

[d.] *Jozef Stefan Institute, Jamova c. 39, SI-1000 Ljubljana, Slovenia*

[e.] *Japan Synchrotron Radiation Facility, SPring-8, Hyogo 679-5198, Japan*

[f.] *RIKEN SPring-8 Center, Hyogo 679-5148, Japan*

[g.] *Faculty of Mathematics and Physics, University of Ljubljana, Jadranska 19, SI-1000 Ljubljana, Slovenia*

[h.] *Department of Physics, Graduate School of Science, Osaka Metropolitan University, Osaka 599-8531, Japan*

[i.] *Faculty of Engineering, Kyoto University of Advanced Science, Kameoka 621-8555, Japan*

Experimental Methods

Synthesis and characterization. The synthesis of $K_xCs_{3-x}C_{60}$ samples with nominal x varying between 0.12 and 2 was performed as follows: stoichiometric quantities of phase-pure powders of K_6C_{60}, Cs_6C_{60} and sublimed C_{60} were mixed, ground, pressed into a pellet, placed in a Ta cell with tightened screw ends and introduced in a Pyrex glass ampoule in an Ar-filled glove box (H_2O < 0.3 ppm, O_2 < 0.1 ppm). After removal from the glove box, the ampoule was evacuated for 30 min before sealing under 400 mbar of He gas pressure. The sealed samples were heated inside a furnace using the following thermal protocol: heating from room temperature to 200°C at 5°C/min; held for 3 hrs; to 300°C at 5°C/min; held for 18 hrs; to 350°C at 5°C/min; held for 5 days, cooling to room temperature at 5°C/min. Once the initial annealing was complete, the product was then removed from the reaction vessel in the glove box, ground, pressed into a pellet, inserted into the same Ta cell for a further period of 6+6+6 days annealing at 430°C with 3 intermediate grindings and pelletizations to improve crystallinity.

Laboratory XRPD using a Bruker D8 ADVANCE with DAVINCI design powder X-ray diffractometer, configured with a Debye-Scherrer geometry and a copper source Cu $K_{\alpha 1}$ = 1.5406 Å was used to routinely check the quality of all intermediate polycrystalline products.

All samples are stable and do not degrade with time as long as they are stored and handled in a strictly moisture- and oxygen-free atmosphere.

Synchrotron X-ray powder diffraction and thermodiffractometry at ambient pressure. All samples were investigated by high-resolution synchrotron X-ray powder diffraction (SXRPD). Diffraction data were collected in continuous scanning mode at various temperatures between 10 and 300 K for samples with nominal compositions, $K_xCs_{3-x}C_{60}$ ($0.12 \leq x \leq 2$) sealed in 0.5-mm dimeter thin-wall glass capillaries under 300 mbar of helium gas and introduced in a helium-flow cryostat with the diffractometer on either the ID31 or the ID22 beamline at the ESRF, Grenoble, France. The wavelengths used for each sample are as follows: x = 0.12: λ = 0.39999 Å at 300 K (ID31); x = 0.25: λ = 0.39999 Å between 40 and 300 K (ID31); x = 0.35: λ = 0.39984 Å at 300 K (ID31); x = 0.5: λ = 0.39984 Å between 10 and 300 K (ID31); x = 0.75: λ = 0.39984 Å between 10 and 300 K (ID31); x = 1: λ = 0.35419 Å at 300 K (ID22); x = 1.5: λ = 0.39996 Å at 300 K (ID31); x = 2: λ = 0.35419 Å at 300 K (ID22). Additional high-resolution SXRPD data were collected at various temperatures between 112 and 300 K (λ = 0.81887 Å) for the sample with nominal K content, x = 1 sealed in a 0.3-mm diameter thin-wall glass capillary under 350 mbar of helium gas with the diffractometer on the BL44B2 beamline at SPring-8, Japan. Data analysis of the SXRPD profiles was performed with the GSAS suite of Rietveld programs. The anomalous contributions, f' and f'' to the X-ray form factors of all atoms were calculated with the program DISPANO and were input into the GSAS

refinements. Cylindrical absorption correction, given as $\mu r/\lambda$ in GSAS, was also applied for each sample (μr = linear absorption coefficient×sample radius, are 0.08-0.1). Thermal displacement parameters of atoms in the majority phases were modelled as isotropic and allowed to refine.

The temperature dependence of the unit cell dimensions – reflecting the anharmonicity of the lattice vibrations – can be accounted for using a Debye model in which the phonon density-of-states is represented by a distribution of phonon frequencies. Fitting of the temperature variation of the unit cell volume, V was performed with the following function [1]:

$$V = V_0 + I_V\, T\, \phi(\Theta_D/T), \quad (1)$$

where V_0 is the unit cell volume at 0 K, Θ_D is the Debye temperature, $I_V = 3k_B\, r\, K\, \gamma$ (K is the isothermal volume compressibility, γ the Grüneisen parameter, r the number of atoms in the primitive cell, and k_B the Boltzmann constant), and $\phi(\Theta_D/T)$ is an approximate analytical function of Θ_D and T valid for $T \geq \Theta_D/10$. The derived parameters from the fits to the thermal expansion data of the studied $K_xCs_{3-x}C_{60}$ compositions are summarized in Table S10.

High-pressure synchrotron X-ray powder diffraction. Pressure-dependent high-resolution SXRPD data were collected at 7 K for samples of composition $K_xCs_{3-x}C_{60}$ with $x_K = 0.35$ ($\lambda = 0.41261$ Å, $P \leq 10.2$ GPa), 0.87 ($\lambda = 0.41238$ Å, $P \leq 9.8$ GPa), and 1.28 ($\lambda = 0.41238$ Å, $P \leq 9.8$ GPa) on beamline BL10XU, SPring-8. The powder samples were loaded in a helium-gas-driven membrane diamond anvil cell (MDAC), which was equipped with stainless steel gasket with a hole 100 μm deep and 200 μm in diameter and placed inside a closed-cycle helium refrigerator. The MDAC diamond culet diameters were 500 μm. Helium gas in the MDAC was used as a pressure medium. The applied pressure was increased at 7 K by controlling the He gas pressure to the membrane of the MDAC with the cell inside the cryostat and was measured with the ruby fluorescence method. Images were collected using a monochromatic beam focused to 40×40 μm^2 on a flat image plate detector (Rigaku R-AXIS IV++, 300×300 mm^2 area, 0.100 mm pixel size) with 2 min exposure time. Masking of the strong Bragg reflections of the diamond anvil and integration of the two-dimensional diffraction images were performed with the WinPIP software. Data analysis of the resulting one-dimensional diffraction profiles was carried out with the GSAS suite of Rietveld analysis programs The same structural model as that used in the Rietveld analysis of the ambient pressure data was employed. There were, however, some differences in the employed methodology: isotropic thermal displacement parameters of carbon were only allowed to refine at the lowest pressure (typically ~0.3 GPa) and then fixed at all other pressures. The K^+/Cs^+ site occupancies in the *fcc* phase were fixed to the values found at ambient pressure and 300 K and were not refined thereafter. No absorption correction was employed, in contrast to the procedure for the ambient pressure data analysis.

The non-linear pressure dependence of the low-temperature unit cell volume of the $K_xCs_{3-x}C_{60}$ compositions as extracted from the Rietveld refinements of the diffraction profiles was fitted with the semiempirical second-order Murnaghan equation-of-state (EoS) [2]:

$$P = (K_0/K'_0)\,[(V_0/V)^{K'_0} - 1], \quad (2)$$

where K_0 is the zero-pressure isothermal bulk modulus, K'_0 is its pressure derivative ($= \mathrm{d}K_0/\mathrm{d}P)_{P=0}$, and V_0 is the unit cell volume at zero pressure (Fig. S20, Table S14). This EoS, whilst having the advantage of algebraic simplicity over other commonly used EoS formulations, models the low-temperature $K_xCs_{3-x}C_{60}$ compressibility data well. The extracted values of K_0 and K'_0 for the x_K = 0.35, 0.87, and 1.28 compositions were used to estimate the corresponding $V(P)$ functions for the x_K = 0.53, 0.64, and 2 compositions, respectively for which no high-pressure diffraction data were available.

Magnetic measurements. Temperature-dependent magnetic susceptibility, χ, was measured at 3 and 5 T under field-cooled (FC) protocol at temperatures between 1.8 and 300 K in order to investigate the magnetic susceptibility behaviour in the normal state. The $\chi(T)$ data were obtained from the difference in magnetization at 5 and 3 T to subtract out adventitious ferromagnetic impurity contributions. Corrections for the core diamagnetic contributions to the susceptibility of C_{60}^{3-} (-2.43×10^{-4} emu mol^{-1}), K^+ and Cs^+ (-0.149×10^{-4} and -0.35×10^{-4} emu mol^{-1}, respectively) were applied to all datasets (Fig. S23).

NMR spectroscopy. ^{39}K and ^{133}Cs NMR spectra of $K_{3-x}Cs_xC_{60}$ samples measured at room temperature are shown in Fig. 1b and S2, respectively. The spectral intensity distribution in both cases reflects the two available alkali metal interstices in the *fcc* structure, namely the larger octahedral (O) and the smaller tetrahedral (T) sites. This is particularly evident in the spectrum of the least-expanded K_3C_{60} phase (Fig. 1b). Notably, however, the ^{133}Cs NMR spectrum of $K_{0.53}Cs_{2.47}C_{60}$ (Fig. S2) shows a shoulder on the high-frequency side of the T-peak. Such a splitting of the T-peak is even more pronounced for the Cs_3C_{60} sample (Fig. S2). This is the so-called T-T' splitting first reported by Walstedt *et al*. in Rb_3C_{60} [3]. We have previously studied as a function temperature in detail the T-T' splitting for Cs_3C_{60} using the magic angle spinning (MAS) NMR technique [4] and demonstrated that it originates from the presence of C_{60}^{3-} merohedral disorder. In $K_{0.53}Cs_{2.47}C_{60}$, in addition to the C_{60}^{3-} merohedral disorder, there is also structural disorder associated with the random occupation of the O-sites by K^+ and Cs^+ ions. The latter results in the broadening of the observed alkali NMR peaks (Fig. S4), but does not entirely remove the inherent T-T' splitting.

The temperature evolution of the ^{133}Cs NMR spectra of $K_{0.53}Cs_{2.47}C_{60}$ is shown in Fig. S24 (left). Both O- and T-peaks initially move at the same rate towards smaller ^{133}Cs shift values with decreasing

temperature – the T-peak shifts from –102 to –174 ppm, while the O-peak from –349 to –429 ppm between room temperature and 180 K. The O-T splitting remains essentially unchanged from 247 ppm at room temperature to 255 ppm at 180 K. However, on further cooling between T' and T_c, the O- and T-peaks behave differently in analogy with our earlier work on the $Rb_xCs_{3-x}C_{60}$ family. In $K_{0.53}Cs_{2.47}C_{60}$, the O-peak remains almost at the same shift between these two temperatures with ^{133}Cs shift changing from –429 to –465 ppm. On the other hand, the T-peak continues to strongly vary from –174 ppm at 180 K to –353 K at T_c. The different temperature dependence of the O- and T-peaks is even more pronounced below T_c whence the frequency of the T-peak decreases with decreasing temperature, while that of the O-peak increases (dashed lines in Fig. S24 (left)). Such a conflicting temperature dependence of the O- and T-peaks in the metallic state may originate from the different temperature-dependent contributions to the alkali-metal chemical shift given by the ring currents on the neighbouring C_{60}^{3-} ions responsible for the extra magnetic field at the two alkali sites [5]. In the overexpanded fullerides studied here, the C_{60}^{3-} dynamics are frozen and the alkali metals make close contacts with the surrounding C_{60} units – thus, ring-current effects are even more pronounced, leading to additional fields, which shift the tightly packed T-sites by an additional ~150 ppm.

A direct consequence of the different temperature dependences of the O- and T-peaks below T' is that these peaks start to overlap considerably (Fig. S24 (left)). Approaching T_c from above, it is spectrally almost impossible to separate the O- and T- peaks. This makes the analysis of ^{133}Cs spin-lattice relaxation rates, $1/T_1$, more complicated, as the two contributions are entangled. In order to address this difficulty, we first analyzed the ^{133}Cs magnetization recovery curves at different resonance frequencies for each temperature assuming single-exponential decay. This gives us a plot of an effective $1/T_1$ value as a function of temperature and shift (Fig. S24 (middle)). Above T' where the O- and T-peaks can be easily separated, $1/T_1T$ for the T-site reduces from 0.051 $s^{-1}K^{-1}$ at room temperature to 0.0462 $s^{-1}K^{-1}$ at 180 K. Between the same two temperatures, $1/T_1T$ for the O-site changes from 0.0081 to 0.0078 $s^{-1}K^{-1}$. The ratio of T_1 values for the T- and O-site thus remains almost the same (6.3 and 5.9 at room temperature and 180 K, respectively). The ratio also remains around 6 below T' – specifically for T = 32 K we find $1/T_1T$ = 0.029 and 0.0047 $s^{-1}K^{-1}$ for the T- and O-sites, respectively, yielding a relaxation rate ratio of 6.1. Therefore, in the final step of two-component ^{133}Cs magnetization recovery analysis, we fixed the ratio between the $1/T_1T$ values for the T- and O-sites to 6, yielding the temperature dependences shown in Fig. 6 and S24 (right).

References

[1] F. Sayetat, P. Fertey, M. Kessler, *J. Appl. Crystallogr.*, 1998, **31**, 121-127.

[2] F. D. Murnaghan, *Am. J. Math.* 1937, **59**, 235-260.

[3] R. E. Walstedt, D. W. Murphy and M. J. Rosseinsky, *Nature*, 1993, **362**, 611-613.

[4] A. Potocnik, A. Y. Ganin, Y. Takabayashi, M. T. McDonald, I. Heinmaa, P. Jeglic, R. Stern, M. J. Rosseinsky, K. Prassides and D. Arcon, *Chem. Sci.*, 2014, **5**, 3008–3017.

[5] A. Pasquarello, M. Schluter and R. C. Haddon, *Science*, 1992, **257**, 1660-1661.

[6] R. H. Zadik, Y. Takabayashi, G. Klupp, R. H. Colman, A. Y. Ganin, A. Potocnik, P. Jeglic, D. Arcon, P. Matus, K. Kamaras, Y. Kasahara, Y. Iwasa, A. N. Fitch, Y. Ohishi, G. Garbarino, K. Kato, M. J. Rosseinsky and K. Prassides, *Sci. Adv.*, 2015, **1**, e1500059.

[7] A. Y. Ganin, Y. Takabayashi, P. Jeglič, D. Arčon, A. Potočnik, P. J. Baker, Y. Ohishi, M. T. McDonald, M. D. Tzirakis, A. McLennan, G. R. Darling, M. Takata, M. J. Rosseinsky and K. Prassides, *Nature*, 2010, **466**, 221–227.

Table S1 Nominal, x, and refined, x_K, K-content, composition of the phase assemblage and ambient temperature *fcc* lattice parameters across the series of $K_xCs_{3-x}C_{60}$ fullerides studied in the present work.

x	x_K	*fcc* phase (%)	*bco* phase (%)	CsC_{60} phase (%)	a_{fcc} (Å)
0.12	0.22(1)	31.5(2)	52.69(7)	14.9(2)	14.7011(2)
0.25	0.35(1)	53.0(2)	40.9(2)	5.7(3)	14.6736(2)
0.35	0.53(1)	54.0(2)	29.9(2)	16.1(3)	14.6262(5)
0.5	0.64(1)	71.21(7)	19.4(2)	9.2(3)	14.6061(2)
0.75	0.87(1)	85.18(7)	14.8(1)	–	14.5576(2)
1	1.28(1)	83.34(4)	16.69(9)	–	14.4611(1)
1.5	1.626(4)	94.05(1)	5.97(7)	–	14.37345(8)
2	1.996(6)	100	–	–	14.28571(7)

Table S2. Refined parameters for the fcc K_2CsC_{60} phase (space group $Fm\bar{3}m$) obtained from the Rietveld analysis of the synchrotron X-ray powder diffraction data collected at 300 K (λ = 0.35419 Å). Estimated errors in the last digits are given in parentheses. The weighted-profile and expected R-factors are R_{wp} = 3.76% and R_{exp} = 2.74%. The lattice constant and unit cell volume are: a = 14.28571(7) Å and V = 2915.45(4) Å^3. The tetrahedral and octahedral cavities were occupied by K and Cs, respectively; the sum of the fractional occupancies of the K and Cs atoms was constrained to 2. This resulted in a refined stoichiometry of the fcc-phase of $K_{1.996(6)}Cs_{1.002(6)}C_{60}$. The C−C bond lengths of the C_{60} units were kept fixed at 1.42 Å.

T = 300 K	x/a	y/b	z/c	M	N	B_{iso} (Å^2)
K	0.25	0.25	0.25	8	0.998(3)	2.05(2)
Cs	0.5	0.5	0.5	4	1.002(3)	3.96(2)
C(1)	0	0.049763	0.241348	96	0.5	1.01(2)
C(2)	0.210662	0.080449	0.099325	192	0.5	1.01(2)
C(3)	0.179774	0.160797	0.049763	192	0.5	1.01(2)

Table S3 Refined parameters for the fcc $K_xCs_{3-x}C_{60}$ phase (nominal x = 1.5, space group $Fm\bar{3}m$, phase fraction refined to 94.05(1)%) obtained from the Rietveld analysis of the synchrotron X-ray powder diffraction data collected at 300 K (λ = 0.39996 Å). Estimated errors in the last digits are given in parentheses. The weighted-profile and expected R-factors are R_{wp} = 4.55% and R_{exp} = 3.41%. The lattice constant and unit cell volume are: a = 14.37345(8) Å and V = 2969.50(5) Å^3. The sum of the fractional occupancies of the K and Cs(1) atoms residing in the tetrahedral holes was constrained to 1; the fractional occupancy of the Cs(2) atom residing in the octahedral hole was fixed to 1. This resulted in a refined stoichiometry of the fcc-phase of $K_{1.626(4)}Cs_{1.374(4)}C_{60}$. The C−C bond lengths of the C_{60} units were kept fixed at 1.42 Å. The fraction of the co-existing body-centred-orthorhombic (space group $Immm$) phase is 5.97(7)%.

T = 300 K	x/a	y/b	z/c	M	N	B_{iso} (Å^2)
K	0.25	0.25	0.25	8	0.813(2)	1.83(2)
Cs(1)	0.25	0.25	0.25	8	0.187(2)	1.83(2)
Cs(2)	0.5	0.5	0.5	4	1.0	5.14(2)
C(1)	0	0.049460	0.239874	96	0.5	0.66(2)
C(2)	0.209376	0.079958	0.098719	192	0.5	0.66(2)
C(3)	0.178677	0.159816	0.049460	192	0.5	0.66(2)

Table S4 Refined parameters for the fcc $K_xCs_{3-x}C_{60}$ phase (nominal $x = 1$, space group $Fm\bar{3}m$, phase fraction refined to 83.34(4)%) obtained from the Rietveld analysis of the synchrotron X-ray powder diffraction data collected at 112 K (λ = 0.81887 Å) and 300 K (λ = 0.35419 Å). Estimated errors in the last digits are given in parentheses. The weighted-profile and expected R-factors are R_{wp} = 3.88% and R_{exp} = 2.82% (300 K) and R_{wp} = 3.91% and R_{exp} = 2.36% (112 K). The lattice constants and unit cell volumes are: a = 14.4611(1) Å and V = 3024.13(7) Å^3 at 300 K and a = 14.4006(1) Å and V = 2986.37(7) Å^3 at 112 K. The sum of the fractional occupancies of the K and Cs(1) atoms residing in the tetrahedral holes was constrained to 1; the fractional occupancy of the Cs(2) atom residing in the octahedral hole was fixed to 1. This resulted in a refined stoichiometry of the fcc-phase of $K_{1.28(1)}Cs_{1.72(1)}C_{60}$, which was kept fixed in subsequent refinements at higher temperatures. The C−C bond lengths of the C_{60} units were kept fixed at 1.42 Å. The fraction of the co-existing body-centred-orthorhombic (space group $Immm$) phase is 16.69(9)%.

T = 112 K	x/a	y/b	z/c	M	N	B_{iso} (Å^2)
K	0.25	0.25	0.25	8	0.641(3)	0.26(1)
Cs(1)	0.25	0.25	0.25	8	0.359(3)	0.26(1)
Cs(2)	0.5	0.5	0.5	4	1.0	1.89(1)
C(1)	0	0.049366	0.239422	96	0.5	0.18(2)
C(2)	0.208981	0.079807	0.098533	192	0.5	0.18(2)
C(3)	0.178340	0.159515	0.049366	192	0.5	0.18(2)
T = 300 K	x/a	y/b	z/c	M	N	B_{iso} (Å^2)
K	0.25	0.25	0.25	8	0.641	1.17(1)
Cs(1)	0.25	0.25	0.25	8	0.359	1.17(1)
Cs(2)	0.5	0.5	0.5	4	1.0	4.12(2)
C(1)	0	0.049159	0.238416	96	0.5	0.78(2)
C(2)	0.208103	0.079472	0.098118	192	0.5	0.78(2)
C(3)	0.177590	0.158844	0.049159	192	0.5	0.78(2)

Table S5 Refined parameters for the fcc $K_xCs_{3-x}C_{60}$ phase (nominal x = 0.75, space group $Fm\bar{3}m$, phase fraction refined to 85.18(7)%) obtained from the Rietveld analysis of the synchrotron X-ray powder diffraction data collected at 10 and 300 K (λ = 0.39984 Å). Estimated errors in the last digits are given in parentheses. The weighted-profile and expected R-factors are R_{wp} = 3.55% and R_{exp} = 2.60% (300 K) and R_{wp} = 3.62% and R_{exp} = 2.89% (10 K). The lattice constants and unit cell volumes are: a = 14.5576(2) Å and V = 3085.1(1) Å^3 at 300 K and a = 14.4584(1) Å and V = 3022.46(6) Å^3 at 10 K. The sum of the fractional occupancies of the K and Cs(1) atoms residing in the tetrahedral holes was constrained to 1; the fractional occupancy of the Cs(2) atom residing in the octahedral hole was fixed to 1. This resulted in a refined stoichiometry of the fcc-phase of $K_{0.87(1)}Cs_{2.13(1)}C_{60}$, which was kept fixed in subsequent refinements at higher temperatures. The C−C bond lengths of the C_{60} units were kept fixed at 1.42 Å. The fraction of the co-existing body-centred-orthorhombic (space group $Immm$) phase is 14.8(1)%.

T = 10 K	x/a	y/b	z/c	M	N	B_{iso} (Å^2)
K	0.25	0.25	0.25	8	0.435(6)	0.59(1)
Cs(1)	0.5	0.5	0.5	4	0.565(6)	0.59(1)
Cs(2)	0.5	0.5	0.5	4	1.0	1.11(1)
C(1)	0	0.045305	0.241300	96	0.5	0.33(2)
C(2)	0.209783	0.082731	0.094550	192	0.5	0.33(2)
C(3)	0.181221	0.157584	0.050230	192	0.5	0.33(2)
T = 300 K	x/a	y/b	z/c	M	N	B_{iso} (Å^2)
K	0.25	0.25	0.25	8	0.435	1.09(3)
Cs(1)	0.25	0.25	0.25	8	0.565	1.09(3)
Cs(2)	0.5	0.5	0.5	4	1.0	4.59(5)
C(1)	0	0.048834	0.236840	96	0.5	0.57(5)
C(2)	0.206727	0.078947	0.097470	192	0.5	0.57(5)
C(3)	0.176417	0.157794	0.048834	192	0.5	0.57(5)

Table S6 Refined parameters for the fcc $K_xCs_{3-x}C_{60}$ phase (nominal x = 0.5, space group $Fm\bar{3}m$, phase fraction refined to 71.21(7)%) obtained from the Rietveld analysis of the synchrotron X-ray powder diffraction data collected at 10 and 300 K (λ = 0.39984 Å). Estimated errors in the last digits are given in parentheses. The weighted-profile and expected R-factors are R_{wp} = 3.04% and R_{exp} = 2.21% (300 K) and R_{wp} = 3.38% and R_{exp} = 2.54% (10 K). The lattice constants and unit cell volumes are: a = 14.6061(2) Å and V = 3116.0(1) Å^3 at 300 K and a = 14.5040(1) Å and V = 3051.15(6) Å^3 at 10 K. The sum of the fractional occupancies of the K and Cs(1) atoms residing in the tetrahedral holes was constrained to 1; the fractional occupancy of the Cs(2) atom residing in the octahedral hole was fixed to 1. This resulted in a refined stoichiometry of the fcc-phase of $K_{0.64(1)}Cs_{2.36(1)}C_{60}$, which was kept fixed in subsequent refinements at higher temperatures. The C−C bond lengths of the C_{60} units were kept fixed at 1.42 Å. The fractions of the co-existing body-centred-orthorhombic (space group $Immm$) and CsC_{60} phases are 19.4(2)% and 9.2(3)%, respectively.

T = 10 K	x/a	y/b	z/c	M	N	B_{iso} (Å^2)
K	0.25	0.25	0.25	8	0.319(5)	0.40(1)
Cs(1)	0.25	0.25	0.25	8	0.681(5)	0.40(1)
Cs(2)	0.5	0.5	0.5	4	1.0	0.84(1)
C(1)	0	0.049014	0.237715	96	0.5	0.22(2)
C(2)	0.207491	0.079238	0.097830	192	0.5	0.22(2)
C(3)	0.177068	0.158377	0.049014	192	0.5	0.22(2)
T = 300 K	x/a	y/b	z/c	M	N	B_{iso} (Å^2)
K	0.25	0.25	0.25	8	0.319	2.02(3)
Cs(1)	0.25	0.25	0.25	8	0.681	2.02(3)
Cs(2)	0.5	0.5	0.5	4	1.0	8.47(4)
C(1)	0	0.04867	0.23605	96	0.5	0.92(4)
C(2)	0.20604	0.07869	0.09715	192	0.5	0.92(4)
C(3)	0.17583	0.15727	0.04867	192	0.5	0.92(4)

Table S7 Refined parameters for the fcc $K_xCs_{3-x}C_{60}$ phase (nominal x = 0.35, space group $Fm\bar{3}m$, phase fraction refined to 54.0(2)%) obtained from the Rietveld analysis of the synchrotron X-ray powder diffraction data collected at 300 K (λ = 0.39984 Å). Estimated errors in the last digits are given in parentheses. The weighted-profile and expected R-factors are R_{wp} = 4.11% and R_{exp} = 2.96%. The lattice constant and unit cell volume are: a = 14.6262(5) Å and V = 3128.9(3) Å^3. The sum of the fractional occupancies of the K and Cs(1) atoms residing in the tetrahedral holes was constrained to 1; the fractional occupancy of the Cs(2) atom residing in the octahedral hole was fixed to 1. This resulted in a refined stoichiometry of the fcc-phase of $K_{0.53(1)}Cs_{2.47(1)}C_{60}$. The C−C bond lengths of the C_{60} units were kept fixed at 1.42 Å. The fractions of the co-existing body-centred-orthorhombic (space group $Immm$) and CsC_{60} phases are 29.9(2)% and 16.1(3)%, respectively.

T = 300 K	x/a	y/b	z/c	M	N	B_{iso} (Å^2)
K	0.25	0.25	0.25	8	0.263(6)	1.17(3)
Cs(1)	0.25	0.25	0.25	8	0.737(6)	1.17(3)
Cs(2)	0.5	0.5	0.5	4	1.0	5.60(4)
C(1)	0	0.048605	0.235729	96	0.5	0.71(4)
C(2)	0.205758	0.078576	0.097013	192	0.5	0.71(4)
C(3)	0.175589	0.157054	0.048605	192	0.5	0.71(4)

Table S8 Refined parameters for the fcc $K_xCs_{3-x}C_{60}$ phase (nominal x = 0.25, space group $Fm\bar{3}m$, phase fraction refined to 53.0(2)%) obtained from the Rietveld analysis of the synchrotron X-ray powder diffraction data collected at 40 and 300 K (λ = 0.39999 Å). Estimated errors in the last digits are given in parentheses. The weighted-profile and expected R-factors are R_{wp} = 5.34% and R_{exp} = 4.47% (300 K) and R_{wp} = 5.41% and R_{exp} = 3.52% (40 K). The lattice constants and unit cell volumes are: a = 14.6736(2) Å and V = 3159.4(1) Å^3 at 300 K and a = 14.5762(3) Å and V = 3096.9(2) Å^3 at 40 K. The sum of the fractional occupancies of the K and Cs(1) atoms residing in the tetrahedral holes was constrained to 1; the fractional occupancy of the Cs(2) atom residing in the octahedral hole was fixed to 1. This resulted in a refined stoichiometry of the fcc-phase of $K_{0.35(1)}Cs_{2.65(1)}C_{60}$, which was kept fixed in subsequent refinements at higher temperatures. The C−C bond lengths of the C_{60} units were kept fixed at 1.42 Å. The fractions of the co-existing body-centred-orthorhombic (space group $Immm$) and CsC_{60} phases are 40.9(2)% and 5.7(3)%, respectively.

T = 40 K	x/a	y/b	z/c	M	N	B_{iso} (Å^2)
K	0.25	0.25	0.25	8	0.176	1.08(3)
Cs(1)	0.25	0.25	0.25	8	0.824	1.08(3)
Cs(2)	0.5	0.5	0.5	4	1.0	2.40(5)
C(1)	0	0.048772	0.236537	96	0.5	0.04(6)
C(2)	0.206463	0.078846	0.097345	192	0.5	0.04(6)
C(3)	0.176191	0.157592	0.048772	192	0.5	0.04(6)
T = 300 K	x/a	y/b	z/c	M	N	B_{iso} (Å^2)
K	0.25	0.25	0.25	8	0.176(7)	2.16(3)
Cs(1)	0.25	0.25	0.25	8	0.824(7)	2.16(3)
Cs(2)	0.5	0.5	0.5	4	1.0	8.61(7)
C(1)	0	0.048448	0.234968	96	0.5	0.53(6)
C(2)	0.205093	0.078323	0.096699	192	0.5	0.53(6)
C(3)	0.175022	0.156547	0.048448	192	0.5	0.53(6)

Table S9 Refined parameters for the fcc $K_xCs_{3-x}C_{60}$ phase (nominal x = 0.12, space group $Fm\bar{3}m$, phase fraction refined to 31.5(2)%) obtained from the Rietveld analysis of the synchrotron X-ray powder diffraction data collected at 300 K (λ = 0.39999 Å). Estimated errors in the last digits are given in parentheses. The weighted-profile and expected R-factors are R_{wp} = 4.90% and R_{exp} = 3.40%. The lattice constant and unit cell volume are: a = 14.7011(2) Å and V = 3177.2(1) Å^3. The sum of the fractional occupancies of the K and Cs(1) atoms residing in the tetrahedral holes was constrained to 1; the fractional occupancy of the Cs(2) atom residing in the octahedral hole was fixed to 1. This resulted in a refined stoichiometry of the fcc-phase of $K_{0.22(1)}Cs_{2.78(1)}C_{60}$. The C−C bond lengths of the C_{60} units were kept fixed at 1.42 Å. The fractions of the co-existing body-centred-orthorhombic (space group $Immm$) and CsC_{60} phases are 52.69(7)% and 14.9(2)%, respectively.

T = 300 K	x/a	y/b	z/c	M	N	B_{iso} (Å^2)
K	0.25	0.25	0.25	8	0.109(6)	1.28(2)
Cs(1)	0.25	0.25	0.25	8	0.891(6)	1.28(2)
Cs(2)	0.5	0.5	0.5	4	1.0	5.82(4)
C(1)	0	0.048357	0.234528	96	0.5	0.29(5)
C(2)	0.204709	0.078176	0.096518	192	0.5	0.29(5)
C(3)	0.174695	0.156254	0.048357	192	0.5	0.29(5)

Table S10 Parameters of the Debye fits to the $V(T)$ data of the $K_xCs_{3-x}C_{60}$ fullerides investigated in the present work. The values of Θ_D for the samples with x_K = 0.35, 0.64, and 0.87 were fixed at that of Cs_3C_{60} from ref. [6] while that for x_K = 1.28 was fixed at that of Rb_2CsC_{60} from ref. [6]

x	x_K	Fitted T range (K)	V_0 (Å^3)	Θ_D (K)	I_V (Å^3 K^{-1})
0	0	30-295	3161.4(7)	218(22)	0.246(7)
0.25	0.35(1)	100-300	3106.2(3)	218	0.239(2)
0.5	0.64(1)	210-300	3063.9(7)	218	0.231(4)
0.75	0.87(1)	265-300	3031.4(6)	218	0.238(1)
1	1.28(1)	110-300	2973.8(2)	152	0.216(2)
x_{Rb} = 2	x_{Rb} = 2	10-570	2962.0(3)	152(6)	0.2293(9)

Table S11 Refined parameters for the fcc $K_{1.28}Cs_{2.72}C_{60}$ phase (space group $Fm\bar{3}m$, phase fraction refined to 82.739(3)%) obtained from the Rietveld analysis of the synchrotron X-ray powder diffraction data collected at 7 K (λ = 0.41238 Å) at 0.3 and 9.8 GPa. Estimated errors in the last digits are given in parentheses. The weighted-profile and expected R-factors are R_{wp} = 0.42% and R_{exp} = 0.39% (0.3 GPa) and R_{wp} = 0.44% and R_{exp} = 0.41% (9.8 GPa). The lattice constants and unit cell volumes are: a = 14.3491(1) Å and V = 2954.43(6) Å^3 at 0.3 GPa and a = 13.5299(3) Å and V = 2476.8(2) Å^3 at 9.8 GPa. The fractional site occupancies of the K and Cs(1) atoms residing in the tetrahedral holes were fixed to values obtained from the analysis of the ambient pressure data (Table S4); the fractional occupancy of the Cs(2) atom residing in the octahedral hole was fixed to 1. The C−C bond lengths of the C_{60} units were kept fixed at 1.42 Å. The fraction of the co-existing body-centred-orthorhombic (space group $Immm$) phase is 17.26(1)% at 0.3 GPa. The thermal displacement parameters of the C atoms could not refine to physically meaningful values, so they were kept fixed. Those of the metal ions in the tetrahedral and octahedral interstitial sites were only refined at 0.3 GPa and kept fixed to these values at all other pressures.

P = 0.3 GPa	*x/a*	*y/b*	*z/c*	*N*	B_{iso} (Å^2)
K	0.25	0.25	0.25	0.64	0.52(3)
Cs(1)	0.25	0.25	0.25	0.36	0.52(3)
Cs(2)	0.5	0.5	0.5	1.0	0.93(3)
C(1)	0	0.04954	0.24028	0.5	0.13
C(2)	0.20973	0.08009	0.09889	0.5	0.13
C(3)	0.17898	0.16009	0.04954	0.5	0.13
P = 9.8 GPa	*x/a*	*y/b*	*z/c*	*N*	B_{iso} (Å^2)
K	0.25	0.25	0.25	0.64	0.52
Cs(1)	0.25	0.25	0.25	0.36	0.52
Cs(2)	0.5	0.5	0.5	1.0	0.93
C(1)	0	0.05254	0.25483	0.5	0.13
C(2)	0.22243	0.08494	0.10487	0.5	0.13
C(3)	0.18981	0.16978	0.05254	0.5	0.13

Table S12 Refined parameters for the fcc $K_{0.87}Cs_{2.13}C_{60}$ phase (space group $Fm\bar{3}m$, phase fraction refined to 84.02(5)%) obtained from the Rietveld analysis of the synchrotron X-ray powder diffraction data collected at 7 K (λ = 0.41238 Å) at 0.3 and 9.8 GPa. Estimated errors in the last digits are given in parentheses. The weighted-profile and expected R-factors are R_{wp} = 0.56% and R_{exp} = 0.39% (0.3 GPa) and R_{wp} = 0.67% and R_{exp} = 0.38% (9.8 GPa). The lattice constants and unit cell volumes are: a = 14.4468(1) Å and V = 3015.19(6) Å^3 at 0.3 GPa and a = 13.5821(3) Å and V = 2505.5(2) Å^3 at 9.8 GPa. The fractional site occupancies of the K and Cs(1) atoms residing in the tetrahedral holes were fixed to values obtained from the analysis of the ambient pressure data (Table S5); the fractional occupancy of the Cs(2) atom residing in the octahedral hole was fixed to 1. The C−C bond lengths of the C_{60} units were kept fixed at 1.42 Å. The fraction of the co-existing body-centred-orthorhombic (space group $Immm$) phase is 16.3(2)% at 0.3 GPa. The thermal displacement parameters of the atoms were only refined at 0.3 GPa and kept fixed to those values at all other pressures.

P = 0.3 GPa	*x/a*	*y/b*	*z/c*	*N*	B_{iso} (Å^2)
K	0.25	0.25	0.25	0.435	0.92(3)
Cs(1)	0.25	0.25	0.25	0.565	0.92(3)
Cs(2)	0.5	0.5	0.5	1.0	1.42(4)
C(1)	0	0.04921	0.23866	0.5	0.44(4)
C(2)	0.20831	0.07955	0.09822	0.5	0.44(4)
C(3)	0.17777	0.15900	0.04920	0.5	0.44(4)
P = 9.8 GPa	*x/a*	*y/b*	*z/c*	*N*	B_{iso} (Å^2)
K	0.25	0.25	0.25	0.435	0.92
Cs(1)	0.25	0.25	0.25	0.565	0.92
Cs(2)	0.5	0.5	0.5	1.0	1.42
C(1)	0	0.05234	0.25385	0.5	0.44
C(2)	0.22158	0.08462	0.10448	0.5	0.44
C(3)	0.18909	0.16913	0.05234	0.5	0.44

Table S13 Refined parameters for the fcc $K_{0.35}Cs_{2.65}C_{60}$ phase (space group $Fm\bar{3}m$, phase fraction refined to 54.3(1)%) obtained from the Rietveld analysis of the synchrotron X-ray powder diffraction data collected at 7 K (λ = 0.41260 Å) at 0.6 and 10.2 GPa. Estimated errors in the last digits are given in parentheses. The weighted-profile and expected R-factors are R_{wp} = 0.45% and R_{exp} = 0.45% (0.6 GPa) and R_{wp} = 0.92% and R_{exp} = 0.45% (10.2 GPa). The lattice constants and unit cell volumes are: a = 14.4742(4) Å and V = 3032.4(3) Å^3 at 0.6 GPa and a = 13.569(2) Å and V = 2498(1) Å^3 at 10.2 GPa. The fractional site occupancies of the K and Cs(1) atoms residing in the tetrahedral holes were fixed to values obtained from the analysis of the ambient pressure data (Table S8); the fractional occupancy of the Cs(2) atom residing in the octahedral hole was fixed to 1. The C−C bond lengths of the C_{60} units were kept fixed at 1.42 Å. The fractions of the co-existing body-centred-orthorhombic (space group $Immm$) and CsC_{60} phases are 35.0(2)% and 10.7(4)%, respectively (0.3 GPa). Thermal displacement parameters of the tetrahedral holes and C atoms were fixed to values refined from the ambient pressure data for the same sample as, with the data quality available, these could not be meaningfully refined together with the profile shape parameters necessary to describe the pressure-induced peak broadening.

P = 0.6 GPa	*x/a*	*y/b*	*z/c*	*N*	B_{iso} (Å^2)
K	0.25	0.25	0.25	0.435	1.08
Cs(1)	0.25	0.25	0.25	0.565	1.08
Cs(2)	0.5	0.5	0.5	1.0	2.84(2)
C(1)	0	0.049115	0.238205	0.5	0.04
C(2)	0.207919	0.079402	0.098032	0.5	0.04
C(3)	0.177433	0.158703	0.049115	0.5	0.04
P = 10.2 GPa	*x/a*	*y/b*	*z/c*	*N*	B_{iso} (Å^2)
K	0.25	0.25	0.25	0.435	1.08
Cs(1)	0.25	0.25	0.25	0.565	1.08
Cs(2)	0.5	0.5	0.5	1.0	2.84(2)
C(1)	0	0.052393	0.254103	0.5	0.04
C(2)	0.221795	0.084701	0.104574	0.5	0.04
C(3)	0.189275	0.169296	0.052393	0.5	0.04

Table S14 Parameters derived from the second-order Murnaghan equation-of-state fits to the 7 K $V(P)$ data of the $K_xCs_{3-x}C_{60}$ fullerides with x_K = 0.35, 0.87, and 1.28 investigated in the present work. The low-temperature literature data for fcc Cs_3C_{60} [7] and Rb_2CsC_{60} [6] are also included for comparison.

x_K	K_0 (GPa)	K'_0 (= $dK_0/dP)_{P=0}$	κ (= $d\ln V/dP$ (GPa^{-1})	V_0 (Å^3)
0	13.7(3)	13.0(3)	0.073(2)	3163.6
0.35	19.0(1)	9.0(1)	0.0526(3)	3120(1)
0.87	17.9(2)	8.94(9)	0.0559(6)	3057(1)
1.28	18.7(6)	8.6(2)	0.053(2)	3008(3)
x_{Rb} = 2	20.9(3)	8.8(2)	0.0479(7)	2961.9

(a)

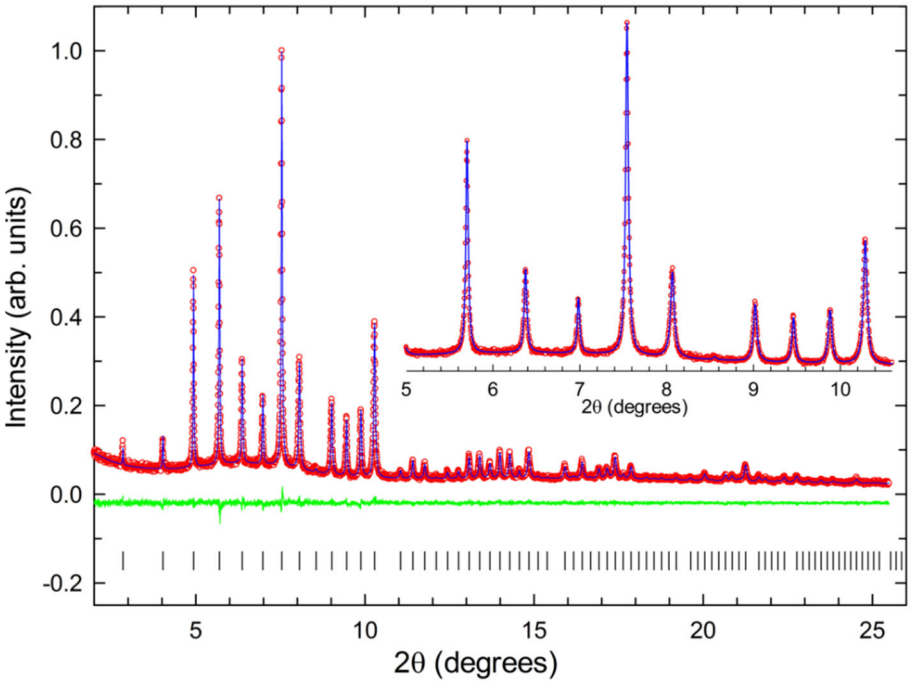

(b)

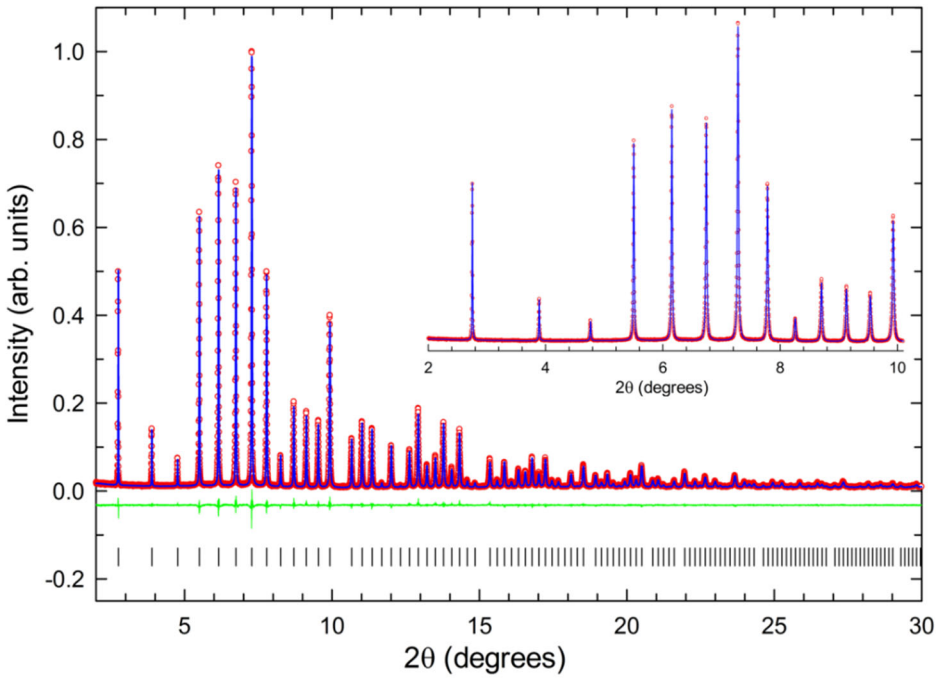

Fig. S1 Rietveld fits to SXRPD data collected at ambient temperature for phase-pure (a) K_6C_{60} (a = 11.3775(2) Å) and (b) Cs_6C_{60} (a = 11.7887(2) Å) (λ = 0.40006 Å, step size = 0.002°). Red circles, blue line and green line represent the observed, calculated and difference profiles, respectively. Black ticks mark the reflection positions of K_6C_{60} and Cs_6C_{60} (space group $Im\bar{3}$). Both insets display expanded regions of the respective diffraction profiles. The weighted-profile and expected R-factors are R_{wp} = 4.43% and R_{exp} = 4.18% (K_6C_{60}) and R_{wp} = 4.43% and R_{exp} = 3.58% (Cs_6C_{60}).

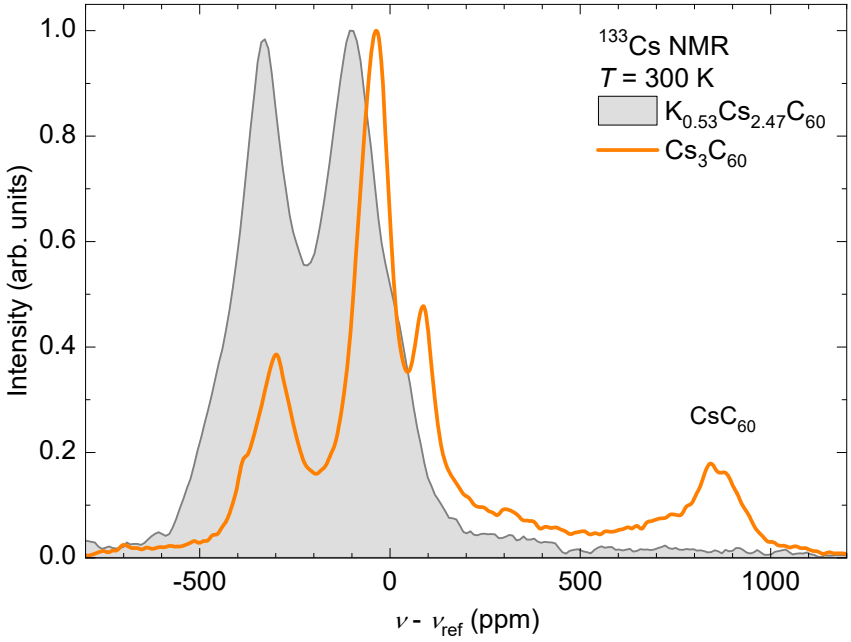

Fig. S2 Comparison of the ^{133}Cs NMR spectra measured for $K_{0.53}Cs_{2.47}C_{60}$ (shaded area) and Cs_3C_{60} (orange line) powders at T = 300 K. Note the presence of the CsC_{60} signal shifted by ~800 ppm relative to reference in the latter sample. The CsC_{60} signal is absent for the $K_{0.53}Cs_{2.47}C_{60}$ sample.

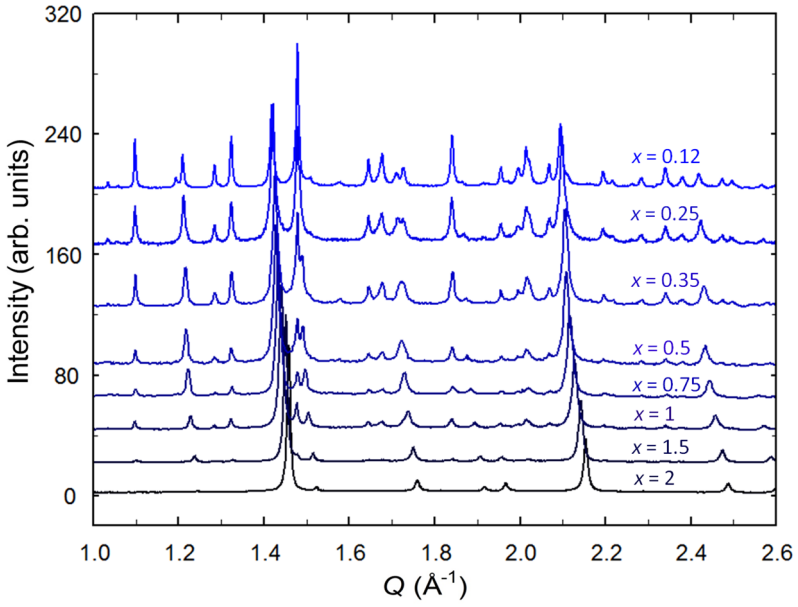

Fig. S3 High-resolution SXRPD profiles collected at ambient temperature for the series of $K_xCs_{3-x}C_{60}$ samples (nominal K content, $0.12 \leq x \leq 2$).

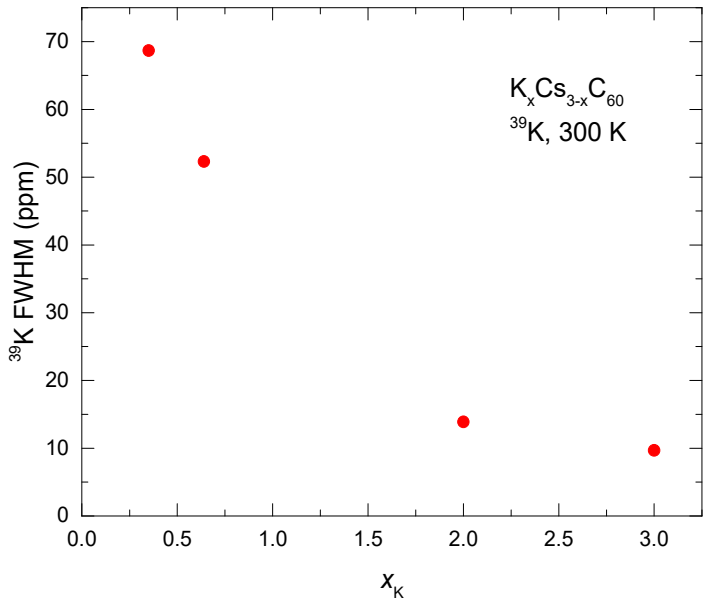

Fig. S4 Full-width-at-half-maximum of the tetrahedral peaks of the ^{39}K NMR spectra of $K_xCs_xC_{60}$ measured at 300 K and plotted against the refined potassium content, x_K.

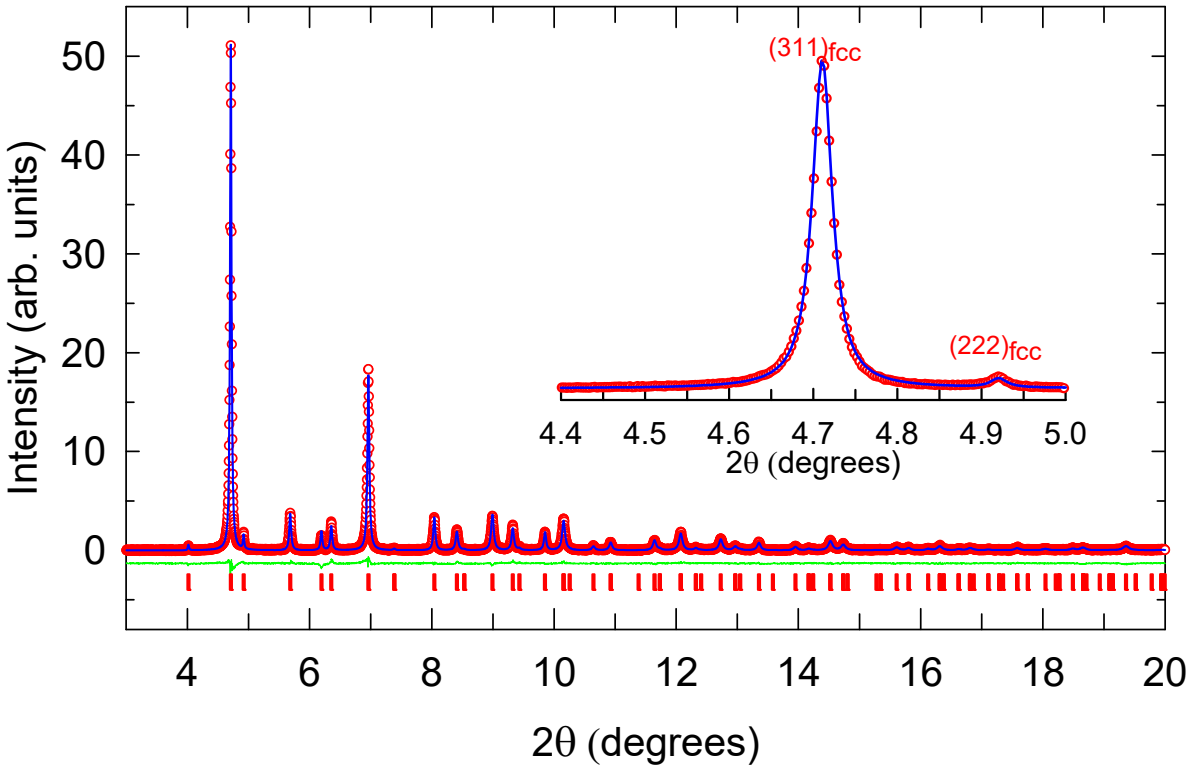

Fig. S5 Rietveld fit to synchrotron XRPD data collected at 300 K for fcc-structured K_2CsC_{60} (R_{wp} = 3.76%, R_{exp} = 2.74%, λ = 0.35419 Å). Red circles, blue lines and green lines represent the observed, calculated and difference profiles. Ticks mark the reflection positions. The inset displays an expanded region of the diffraction profile; observed Bragg peaks are labelled by their *hkl* Miller indices.

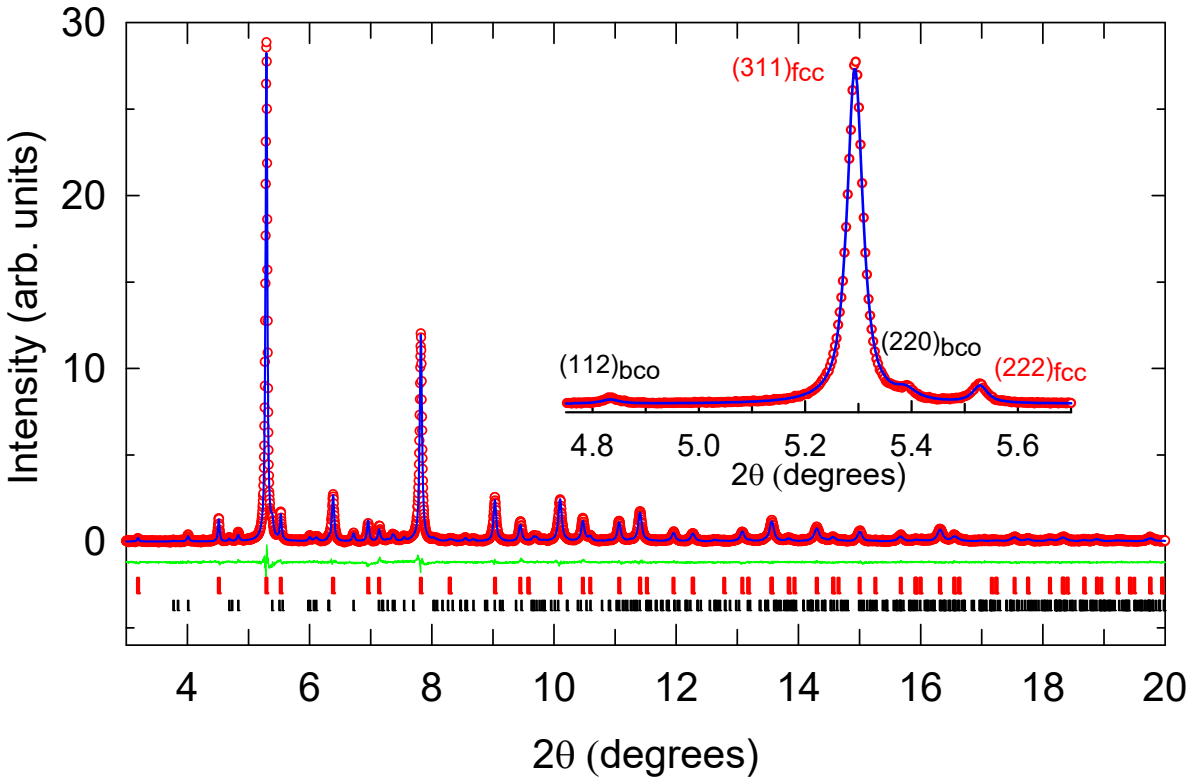

Fig. S6 Rietveld fit to synchrotron XRPD data collected at 300 K for fcc-structured $K_{1.63}Cs_{0.37}C_{60}$ (R_{wp} = 4.55%, R_{exp} = 3.41%, λ = 0.39996 Å). Red circles, blue lines and green lines represent the observed, calculated and difference profiles, respectively. Ticks mark the reflection positions, from top-to-bottom, of co-existing fcc (red ticks, 94.05(1)%) and body-centred-orthorhombic (bco, black ticks, 5.97(7)%) phases. The inset displays an expanded region of the diffraction profile; observed Bragg peaks are labelled by their *hkl* Miller indices.

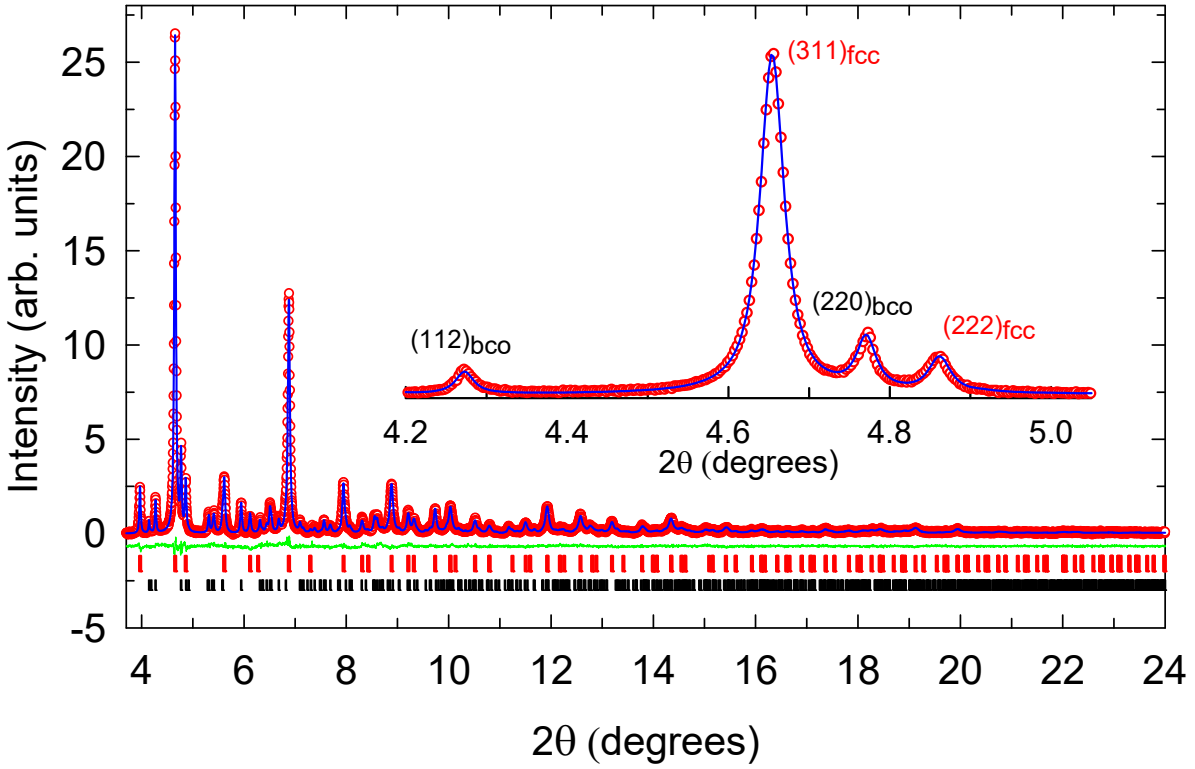

Fig. S7 Rietveld fit to synchrotron XRPD data collected at 300 K for fcc-structured $K_{1.28}Cs_{0.72}C_{60}$ (R_{wp} = 3.88%, R_{exp} = 2.82%, λ = 0.354197 Å). Red circles, blue lines and green lines represent the observed, calculated and difference profiles, respectively. Ticks mark the reflection positions, from top-to-bottom, of co-existing fcc (red ticks, 83.34(4)%) and body-centred-orthorhombic (bco, black ticks, 16.69(9)%) phases. The inset displays an expanded region of the diffraction profile; observed Bragg peaks are labelled by their *hkl* Miller indices.

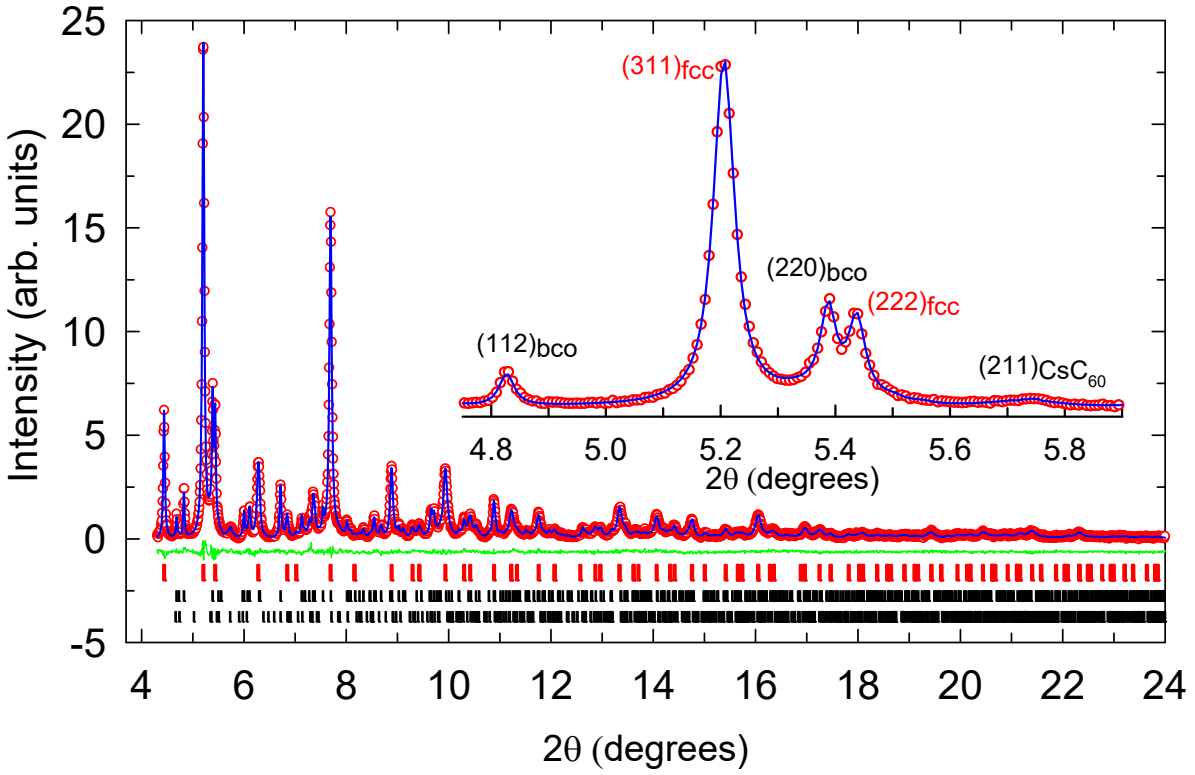

Fig. S8 Rietveld fit to synchrotron XRPD data collected at 300 K for fcc-structured $K_{0.64}Cs_{2.36}C_{60}$ (R_{wp} = 3.04%, R_{exp} = 2.21%, λ = 0.39984 Å). Red circles, blue lines and green lines represent the observed, calculated and difference profiles, respectively. Ticks mark the reflection positions, from top-to-bottom, of co-existing fcc (red ticks, 71.21(7)%), body-centred-orthorhombic (bco, mid black ticks, 19.4(2)%) and CsC_{60} (lower black ticks, 9.2(3)%) phases. The inset displays an expanded region of the diffraction profile; observed Bragg peaks are labelled by their *hkl* Miller indices.

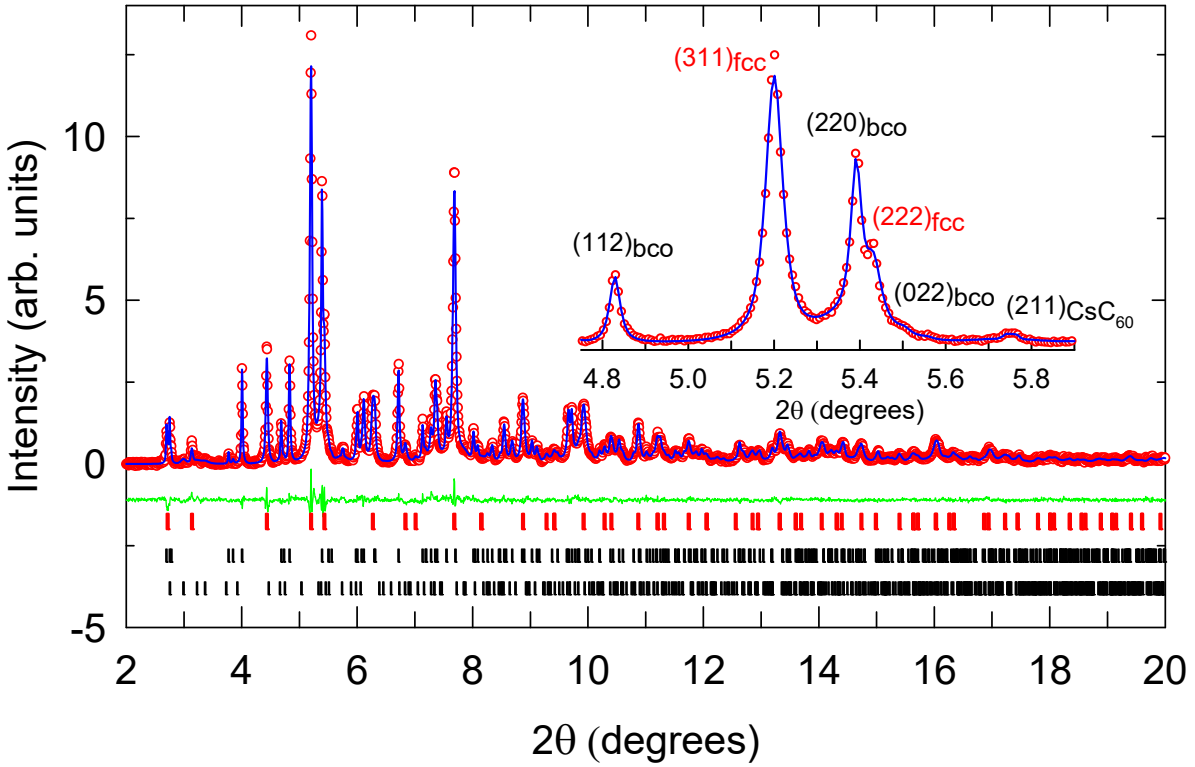

Fig. S9 Rietveld fit to synchrotron XRPD data collected at 300 K for fcc-structured $K_{0.53}Cs_{2.47}C_{60}$ (R_{wp} = 4.11%, R_{exp} = 2.96%, λ = 0.39984 Å). Red circles, blue lines and green lines represent the observed, calculated and difference profiles, respectively. Ticks mark the reflection positions, from top-to-bottom, of co-existing fcc (red ticks, 54.0(2)%), body-centred-orthorhombic (bco, mid black ticks, 29.9(2)%) and CsC_{60} (lower black ticks, 16.1(3)%) phases. The inset displays an expanded region of the diffraction profile; observed Bragg peaks are labelled by their *hkl* Miller indices.

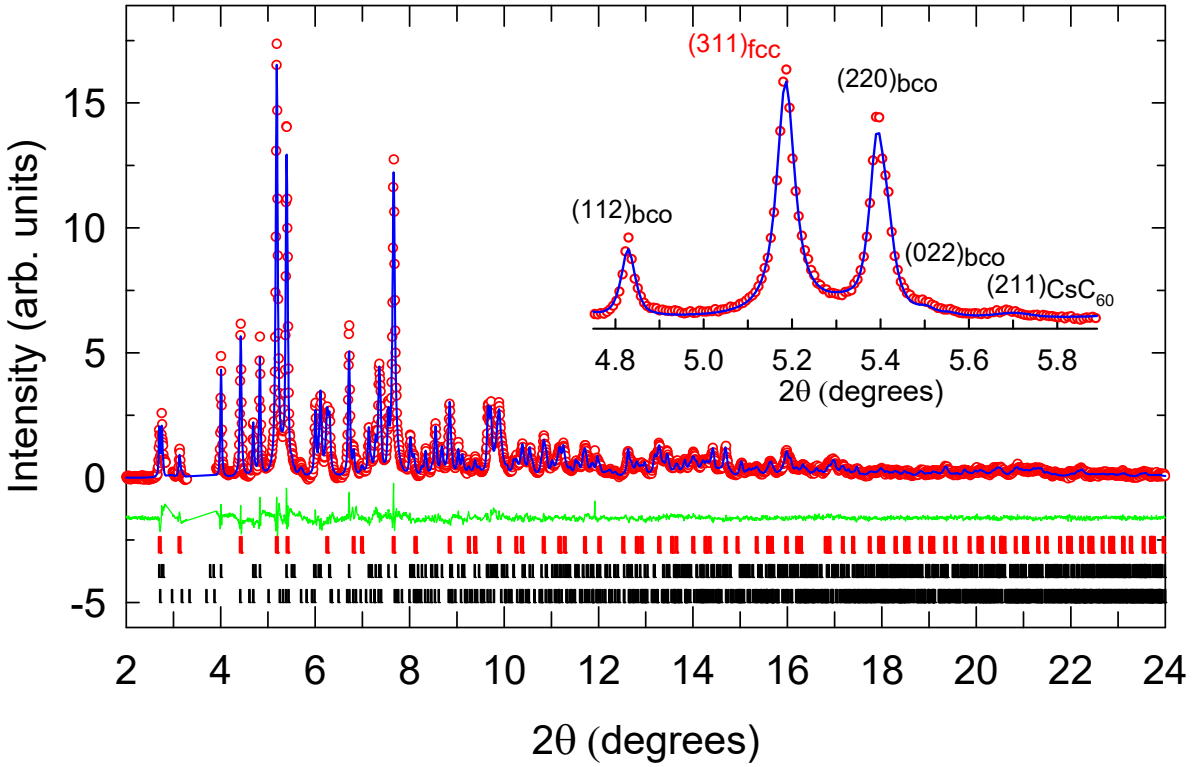

Fig. S10 Rietveld fit to synchrotron XRPD data collected at 300 K for fcc-structured $K_{0.35}Cs_{2.65}C_{60}$ (R_{wp} = 5.34%, R_{exp} = 4.47%, λ = 0.39999 Å). Red circles, blue lines and green lines represent the observed, calculated and difference profiles, respectively. Ticks mark the reflection positions, from top-to-bottom, of co-existing fcc (red ticks, 53.0(2)%), body-centred-orthorhombic (bco, mid black ticks, 40.9(2)%) and CsC_{60} (lower black ticks, 5.7(3)%) phases. The inset displays an expanded region of the diffraction profile; observed Bragg peaks are labelled by their *hkl* Miller indices. Two broad peaks arising from the cryostat were visible at low angles (<4°) and these regions were excluded from the fitting.

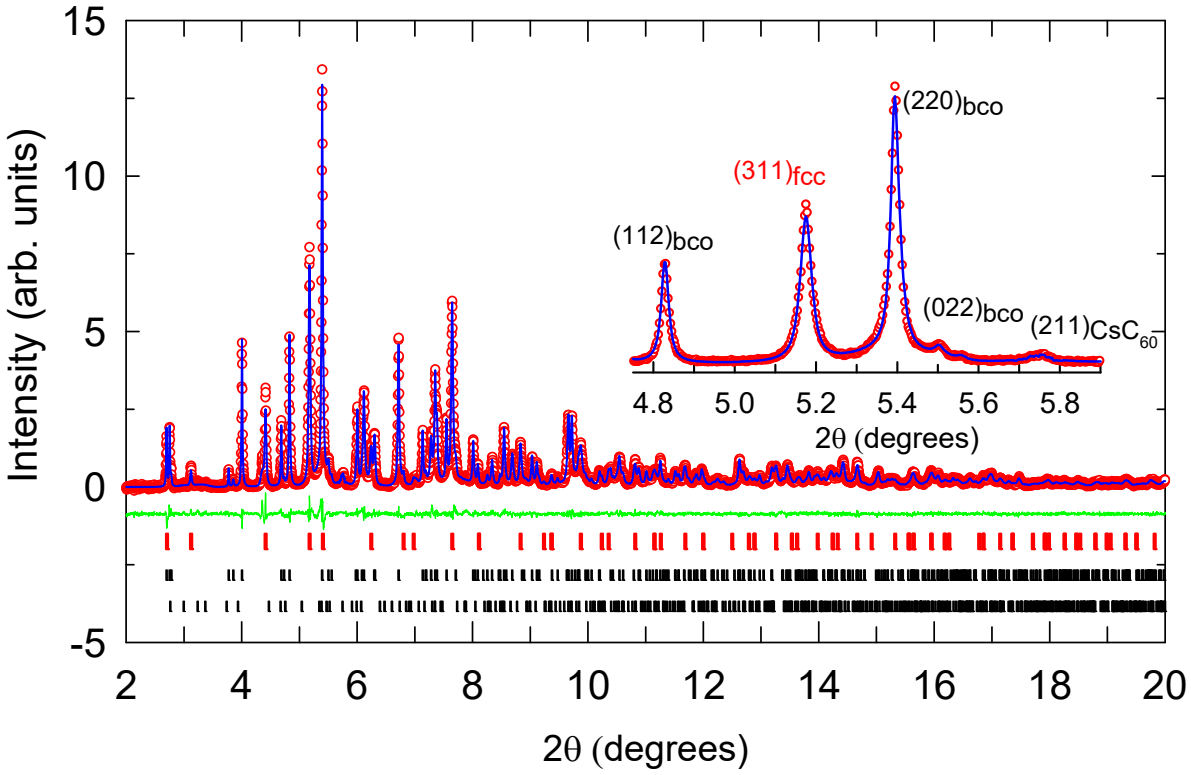

Fig. S11 Rietveld fit to synchrotron XRPD data collected at 300 K for fcc-structured $K_{0.22}Cs_{2.78}C_{60}$ (R_{wp} = 4.90%, R_{exp} = 3.40%, λ = 0.39999 Å). Red circles, blue lines and green lines represent the observed, calculated and difference profiles, respectively. Ticks mark the reflection positions, from top-to-bottom, of co-existing fcc (red ticks, 31.5(2)%), body-centred-orthorhombic (bco, mid black ticks, 52.69(7)%) and CsC_{60} (lower black ticks, 14.9(2)%) phases. The inset displays an expanded region of the diffraction profile; observed Bragg peaks are labelled by their *hkl* Miller indices.

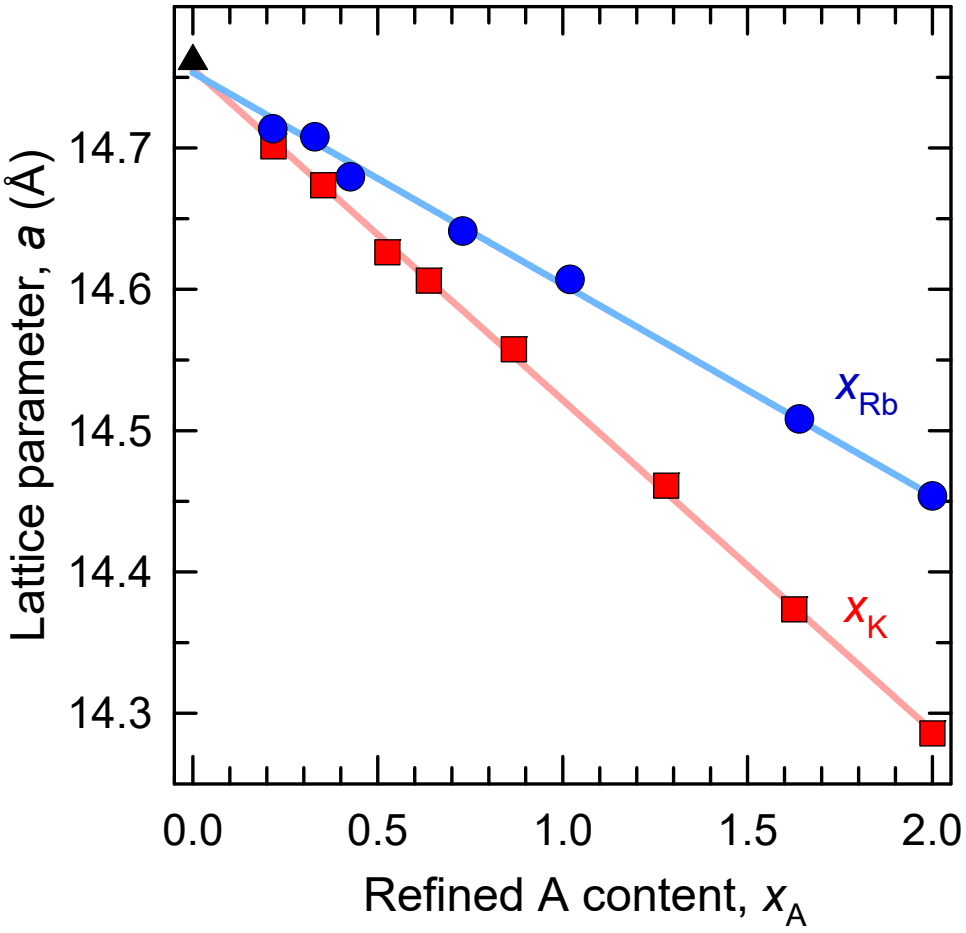

Fig. S12 Variation of the ambient temperature *fcc* lattice parameter of $A_xCs_{3-x}C_{60}$ ($0 \le x \le 2$) with refined A (A = K, Rb) content, x_A. The $x = 0$ (black triangle) and the $Rb_xCs_{3-x}C_{60}$ (blue circles) data are from ref. [7] and [6], respectively. The solid lines are linear fits to the data.

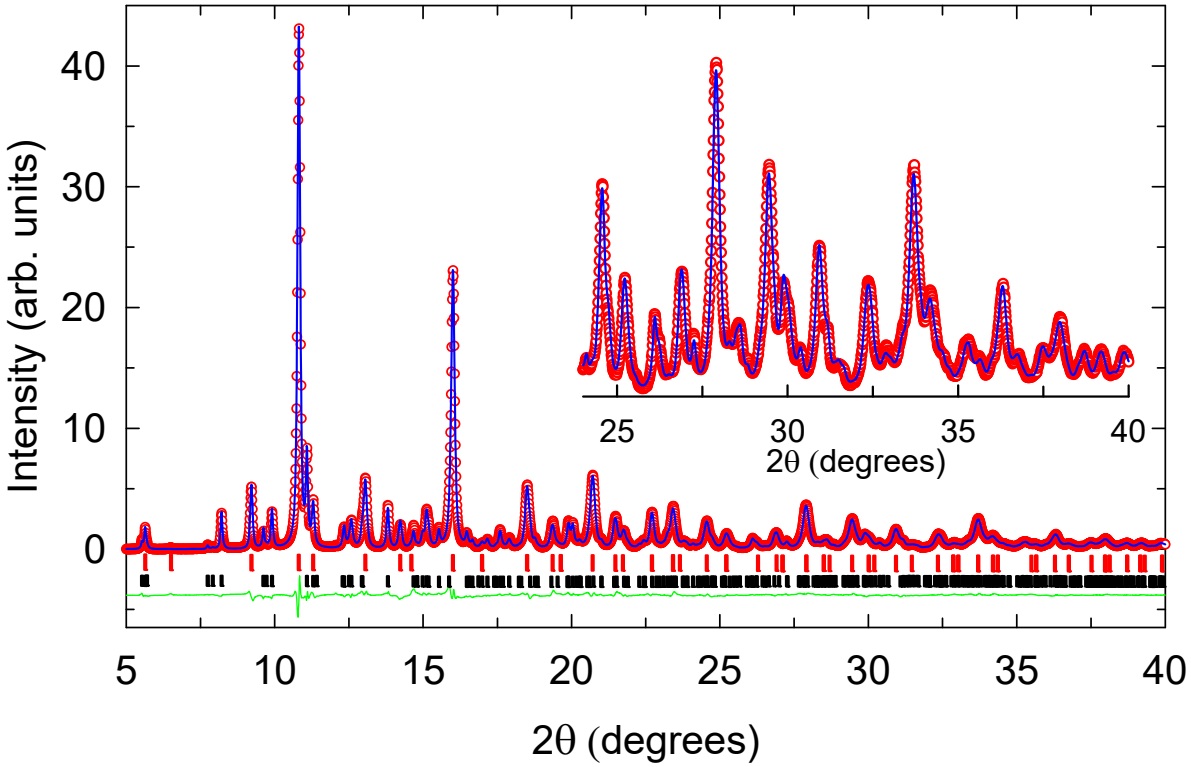

Fig. S13 Rietveld fit to synchrotron XRPD data collected at 112 K for fcc-structured $K_{1.28}Cs_{1.72}C_{60}$ (R_{wp} = 3.91%, R_{exp} = 2.36%, λ = 0.81887 Å). Red circles, blue lines and green lines represent the observed, calculated and difference profiles, respectively. Ticks mark the reflection positions, from top-to-bottom, of co-existing fcc (red ticks) and body-centred-orthorhombic (bco, black ticks) phases. Co-existing phase fractions fixed to values refined from the 300 K dataset. The inset displays an expanded region of the diffraction profile at high angles.

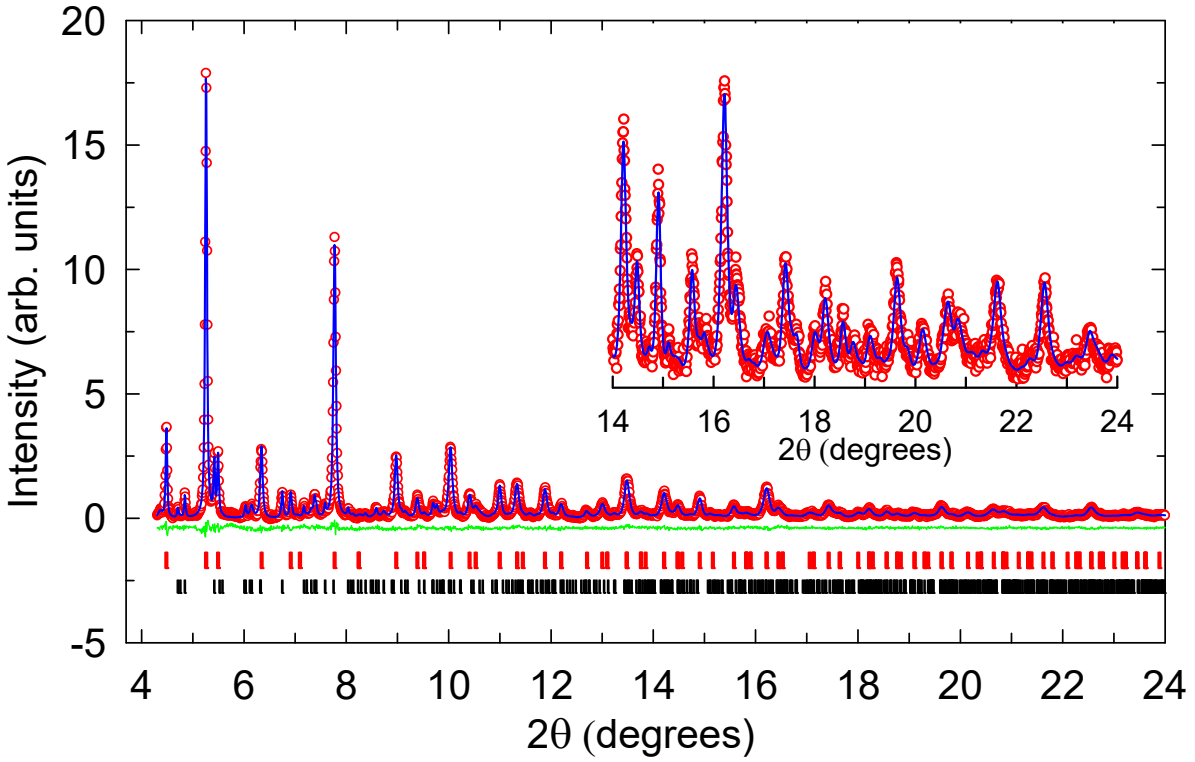

Fig. S14 Rietveld fit to synchrotron XRPD data collected at 10 K for fcc-structured $K_{0.87}Cs_{2.13}C_{60}$ (R_{wp} = 3.62%, R_{exp} = 2.89%, λ = 0.39984 Å). Red circles, blue lines and green lines represent the observed, calculated and difference profiles, respectively. Ticks mark the reflection positions, from top-to-bottom, of co-existing fcc (red ticks) and body-centred-orthorhombic (bco, black ticks) phases. Co-existing phase fractions fixed to values refined from the 300 K dataset. The inset displays an expanded region of the diffraction profile at high angles.

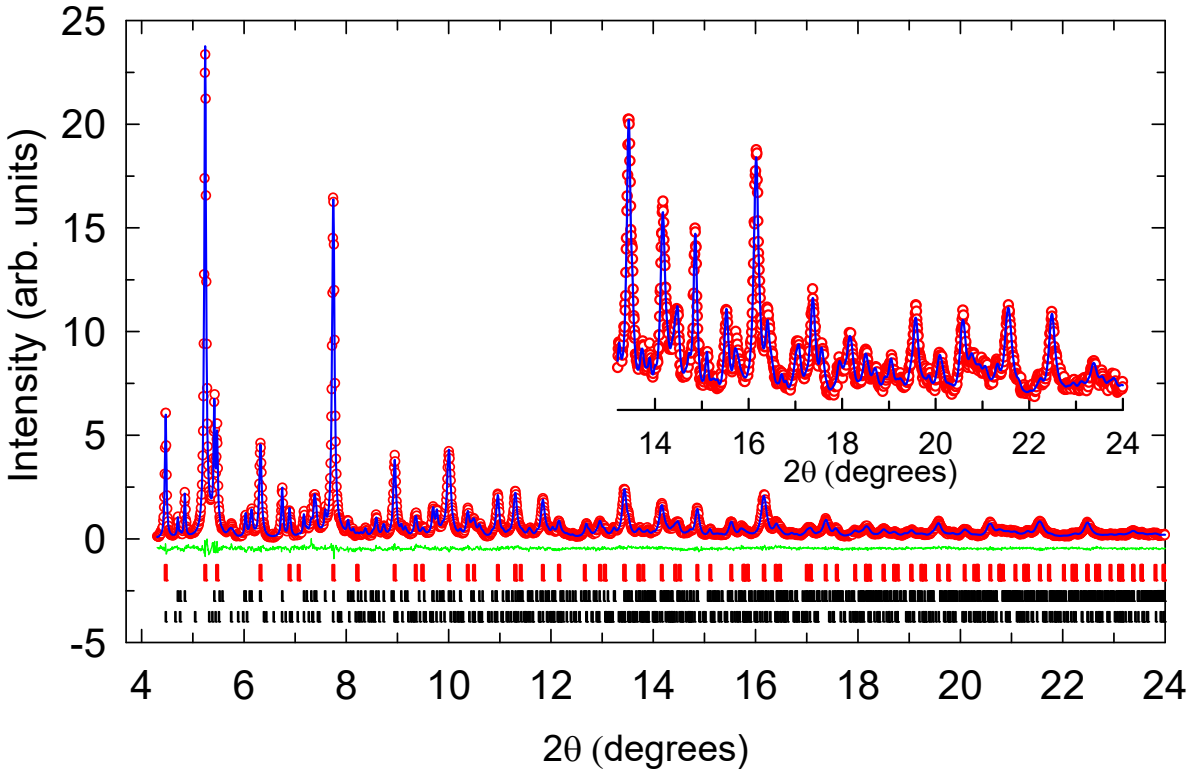

Fig. S15 Rietveld fit to synchrotron XRPD data collected at 10 K for fcc-structured $K_{0.64}Cs_{2.36}C_{60}$ (R_{wp} = 3.38%, R_{exp} = 2.54%, λ = 0.39984 Å). Red circles, blue lines and green lines represent the observed, calculated and difference profiles, respectively. Ticks mark the reflection positions, from top-to-bottom, of co-existing fcc (red ticks), body-centred-orthorhombic (bco, mid black ticks) and CsC_{60} (lower black ticks) phases. Co-existing phase fractions fixed to values refined from the 300 K dataset. The inset displays an expanded region of the diffraction profile at high angles.

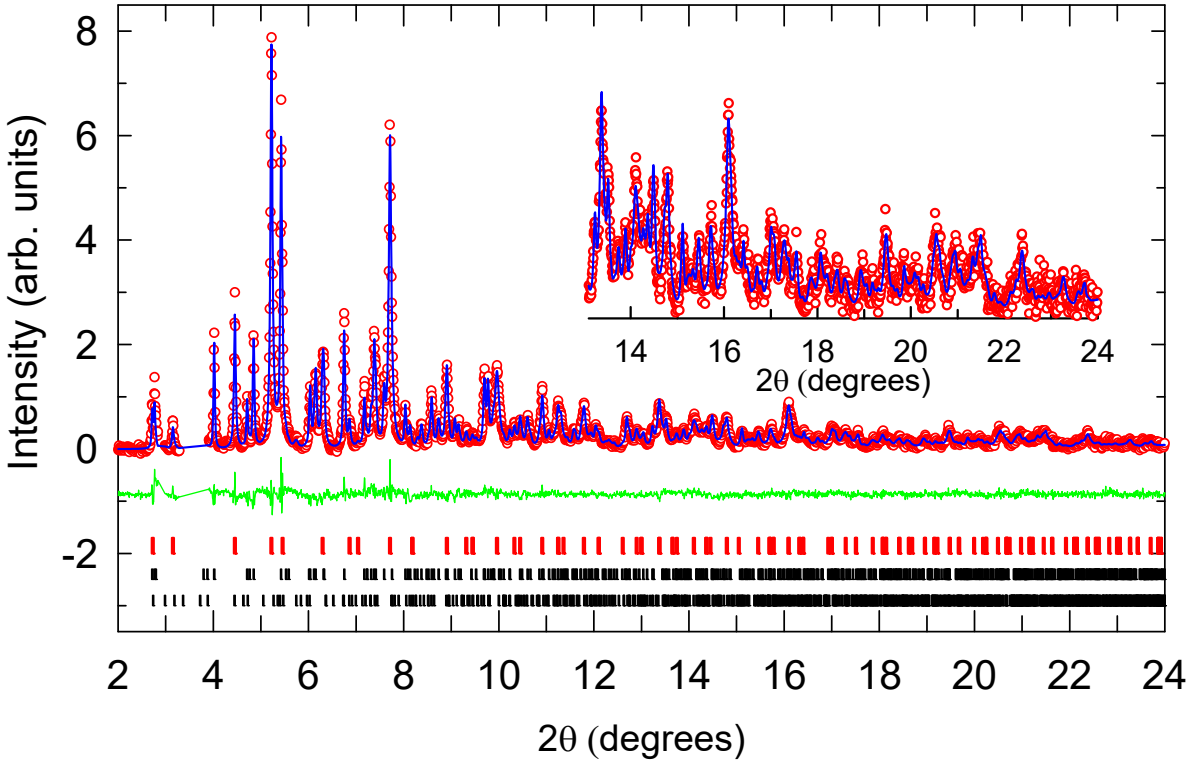

Fig. S16 Rietveld fit to synchrotron XRPD data collected at 40 K for fcc-structured $K_{0.35}Cs_{2.65}C_{60}$ (R_{wp} = 5.41%, R_{exp} = 3.52%, λ = 0.39999 Å). Red circles, blue lines and green lines represent the observed, calculated and difference profiles, respectively. Ticks mark the reflection positions, from top-to-bottom, of co-existing fcc (red ticks), body-centred-orthorhombic (bco, mid black ticks) and CsC_{60} (lower black ticks) phases. Co-existing phase fractions fixed to values refined from the 300 K dataset. Two broad peaks arising from the cryostat were visible at low angles (<4°), and these regions were excluded from the fitting. The inset displays an expanded region of the diffraction profile at high angles.

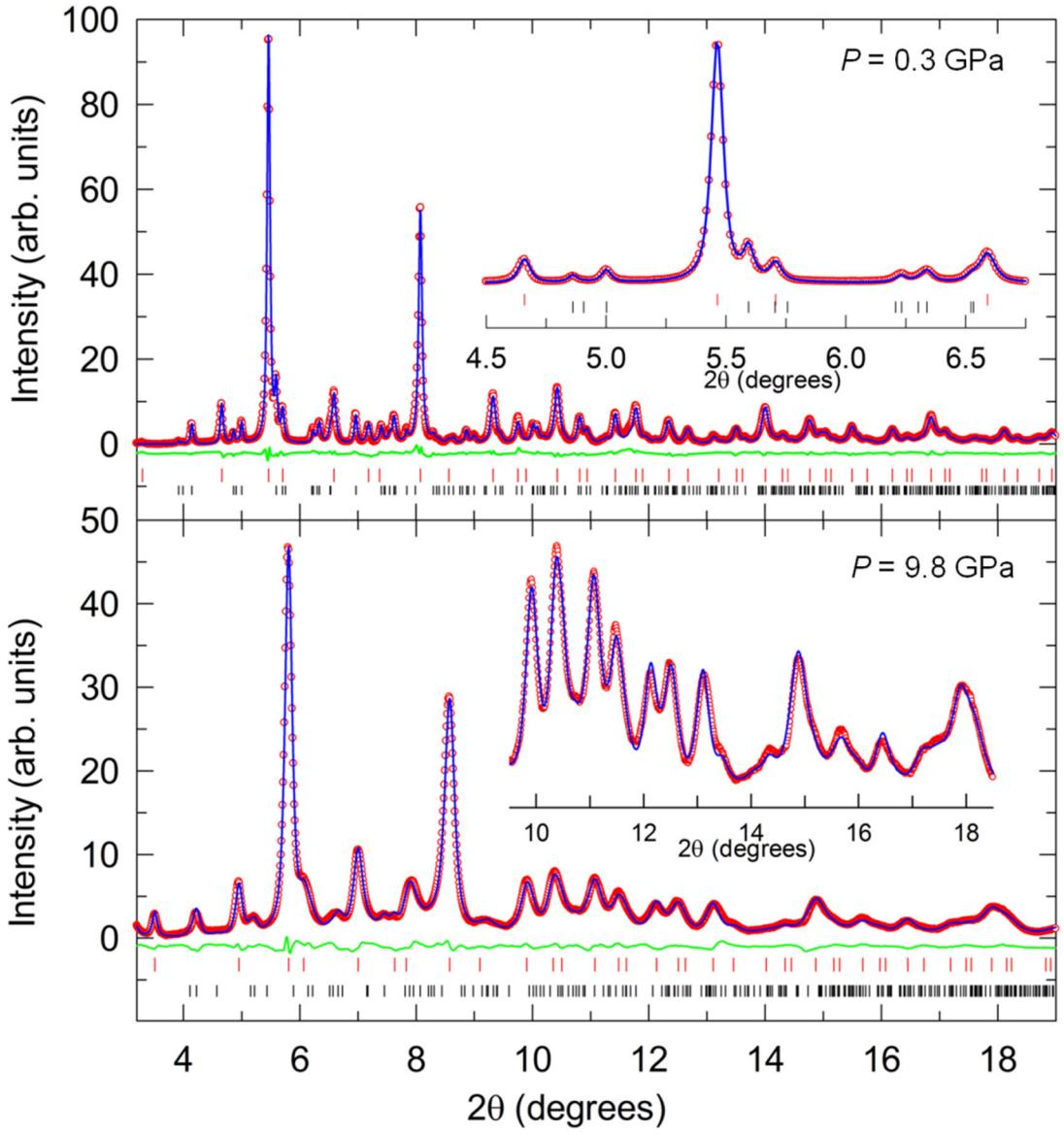

Fig. S17 Rietveld fits to high-pressure synchrotron XRPD data collected at 7 K for fcc-structured $K_{1.28}Cs_{1.72}C_{60}$ at 0.3 GPa (upper panel) and 9.8 GPa (lower panel) (R_{wp} = 0.42%, R_{exp} = 0.39% and R_{wp} = 0.44%, R_{exp} = 0.41%, respectively; λ = 0.41238 Å). Red circles, blue lines and green lines represent the observed, calculated and difference profiles. Ticks mark the reflection positions of co-existing fcc (red ticks) and body-centred-orthorhombic (bco, black ticks) phases. The insets display expanded regions of the respective diffraction profiles at low and high Bragg angles, respectively. The fitted background contribution has been subtracted for clarity.

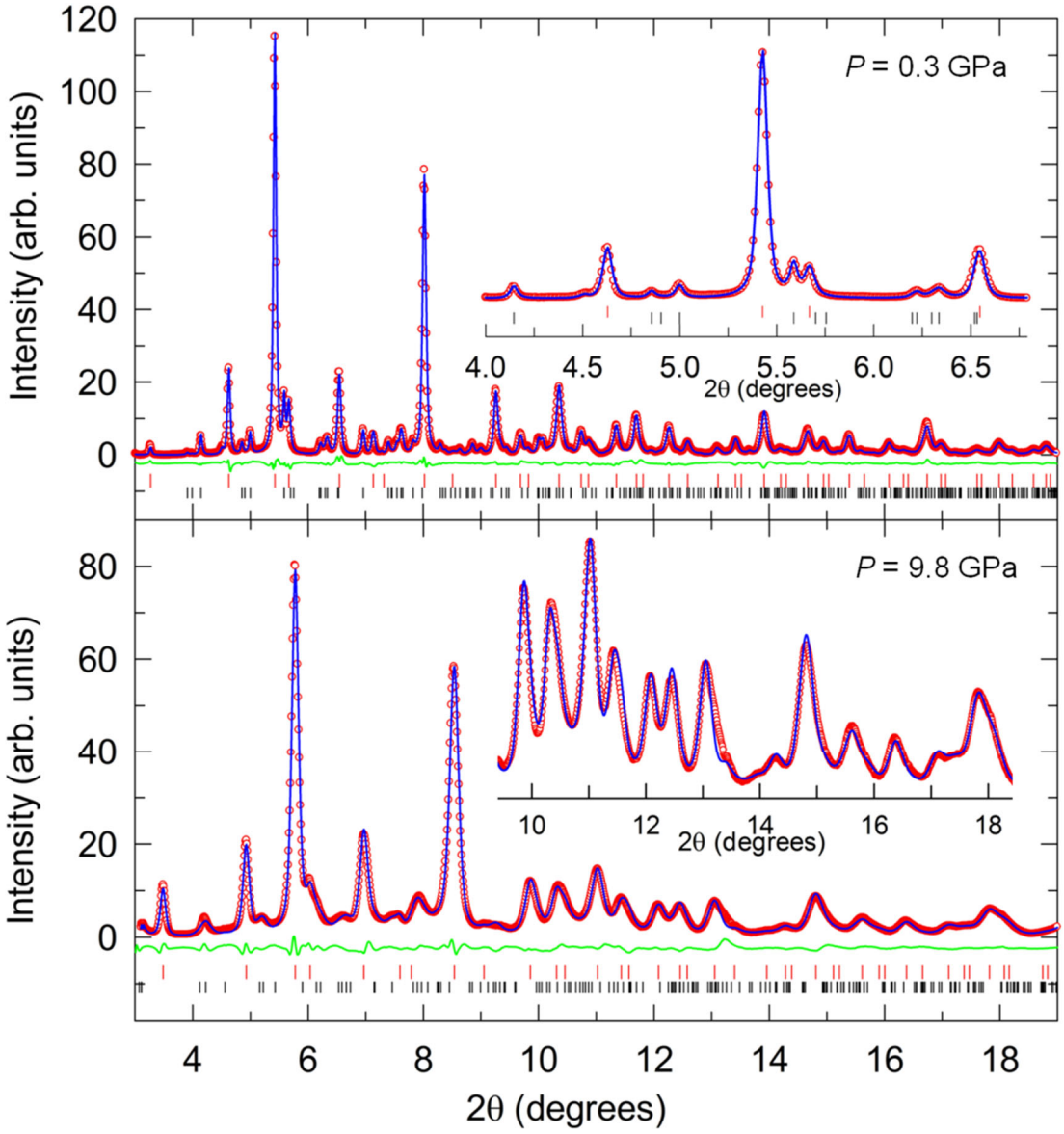

Fig. S18 Rietveld fits to high-pressure synchrotron XRPD data collected at 7 K for fcc-structured $K_{0.87}Cs_{2.13}C_{60}$ at 0.3 GPa (upper panel) and 9.8 GPa (lower panel) (R_{wp} = 0.56%, R_{exp} = 0.39% and R_{wp} = 0.67%, R_{exp} = 0.38%, respectively; λ = 0.41238 Å). Red circles, blue lines and green lines represent the observed, calculated and difference profiles. Ticks mark the reflection positions of co-existing fcc (red ticks) and body-centred-orthorhombic (bco, black ticks) phases. The insets display expanded regions of the respective diffraction profiles at low and high Bragg angles, respectively. The fitted background contribution has been subtracted for clarity.

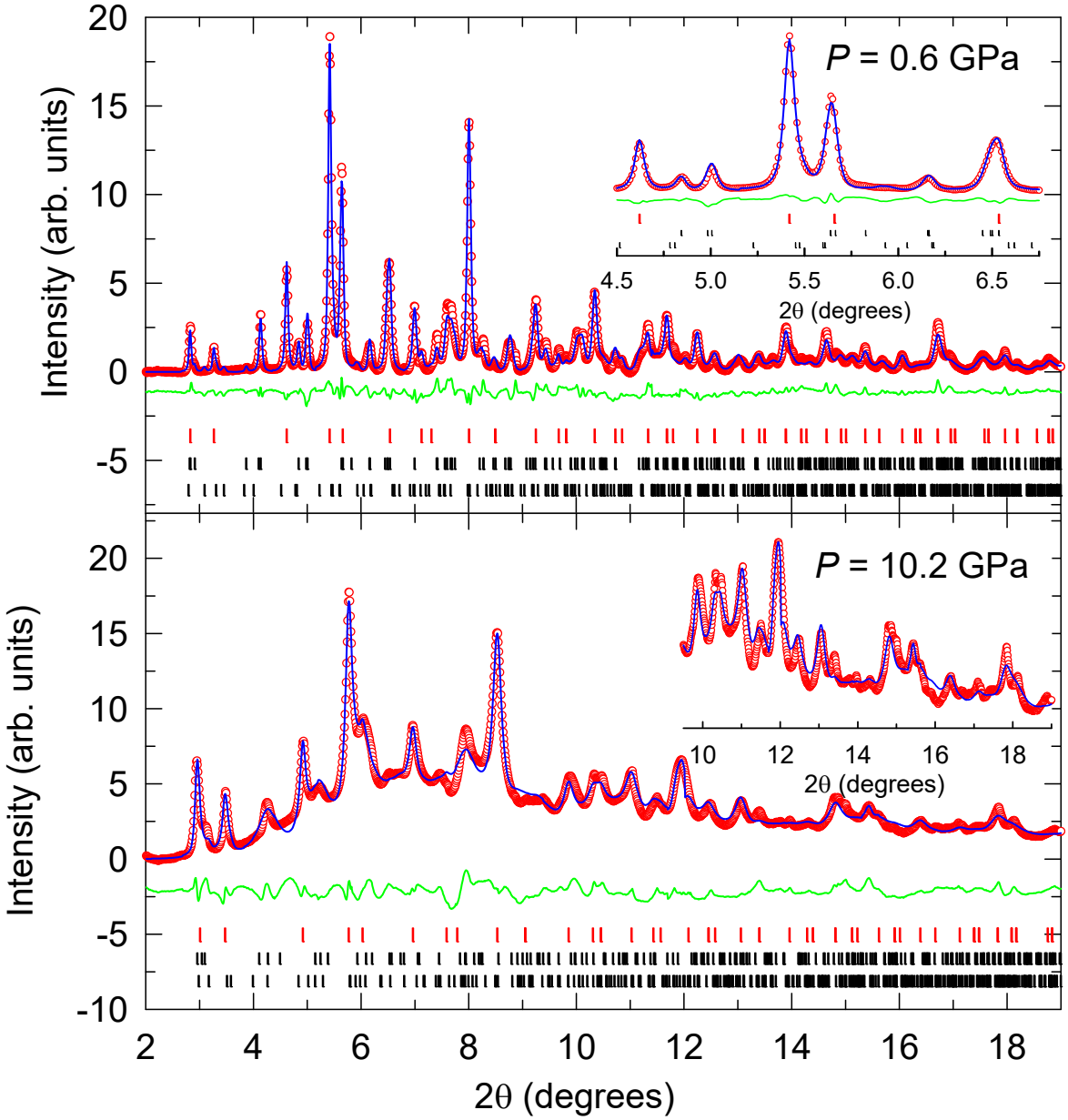

Fig. S19 Rietveld fits to high-pressure synchrotron XRPD data collected at 7 K for fcc-structured $K_{0.35}Cs_{2.65}C_{60}$ at 0.6 GPa (upper panel) and 10.2 GPa (lower panel) (R_{wp} = 0.45%, R_{exp} = 0.45% and R_{wp} = 0.92%, R_{exp} = 0.45%, respectively; λ = 0.41261 Å). Red circles, blue lines and green lines represent the observed, calculated and difference profiles. Ticks mark the reflection positions of co-existing fcc (red ticks), body-centred-orthorhombic (bco, mid black ticks), and CsC_{60} (lower black ticks) phases. The insets display expanded regions of the respective diffraction profiles at low and high Bragg angles, respectively. The fitted background contribution has been subtracted for clarity.

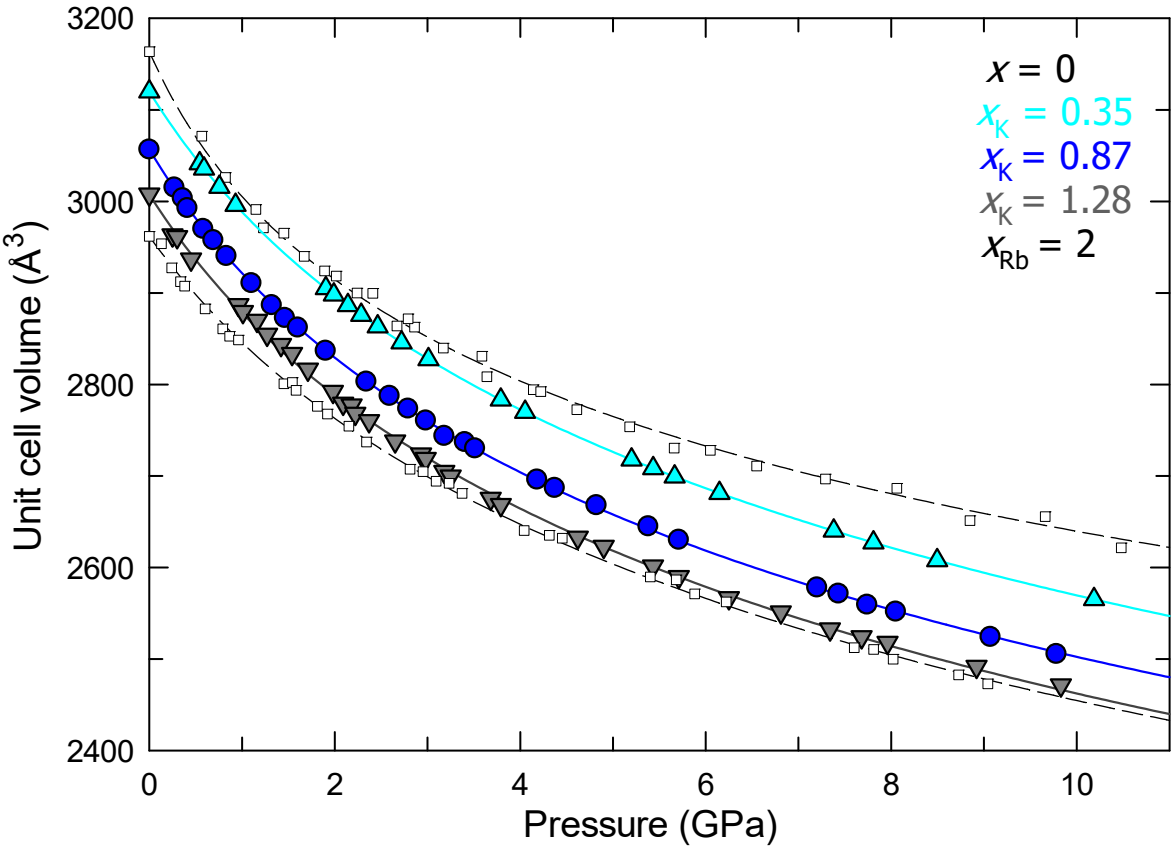

Fig. S20 Pressure dependence of the 7 K unit cell volume of $K_xCs_{3-x}C_{60}$ (x_K = 0.35, 0.87, and 1.28). Data for fcc-structured Cs_3C_{60} at 15 K (dashed line through squares) from ref. [7] and for Rb_2CsC_{60} at 7 K (dashed line through squares) from ref. [6] are also included for comparison. The lines through the data points for the $K_xCs_{3-x}C_{60}$ family are the results of least-squares fits to second-order Murnaghan equations-of-state with zero-pressure isothermal bulk moduli, K_0 of 19.0(1), 17.9(2), and 18.7(6) GPa, and pressure derivatives, K'_0 of 9.0(1), 8.94(9), and 8.6(2) for x_K = 0.35, 0.87, and 1.28, respectively (Table S14). Statistical errors in V from Rietveld analysis are smaller than the data point size.

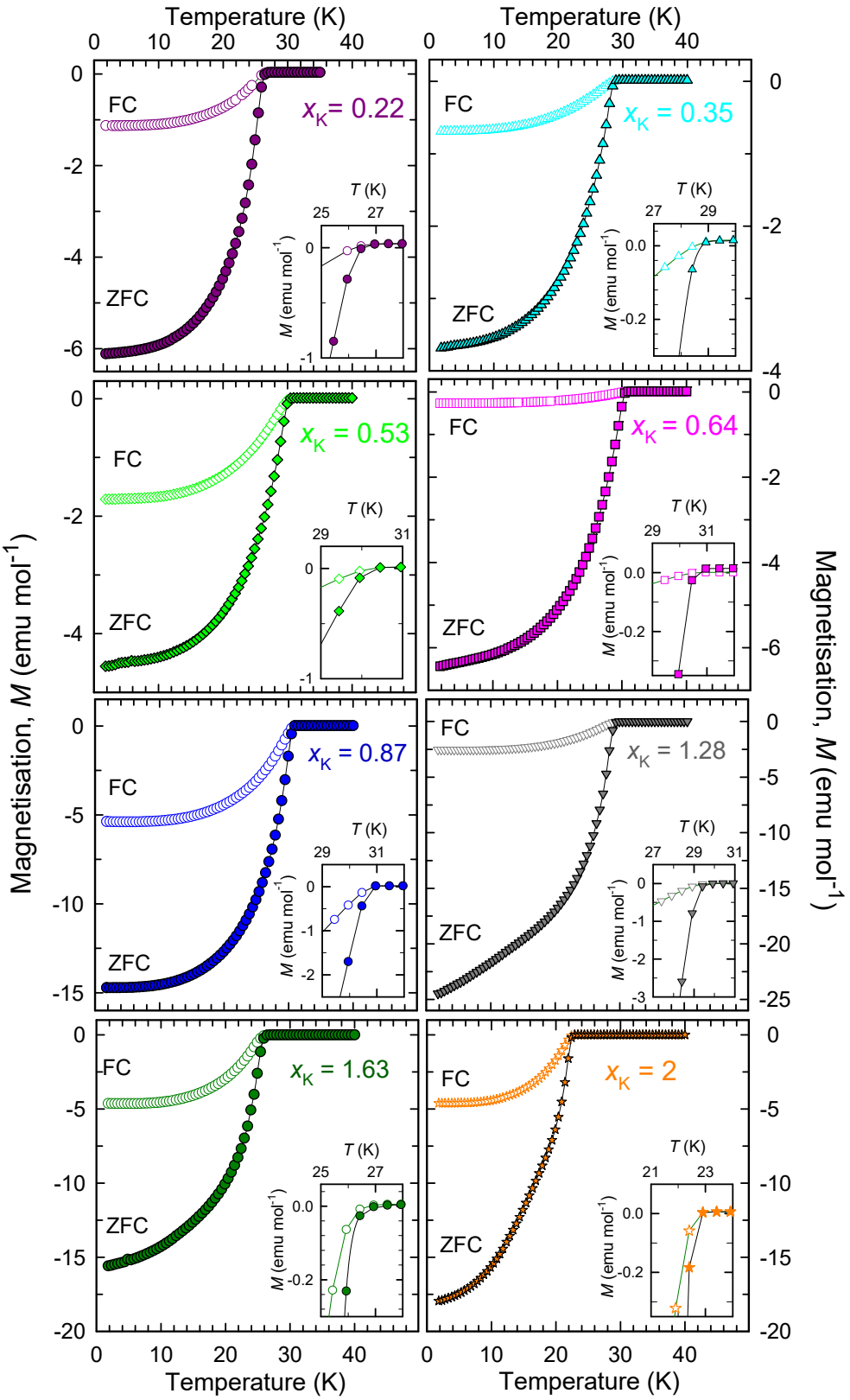

Fig. S21 Temperature dependence of the ZFC and FC magnetisation, M, of the $K_xCs_{3-x}C_{60}$ samples divided by the applied magnetic field. The insets show expanded regions of the respective $M(T)$ data near the superconducting T_c.

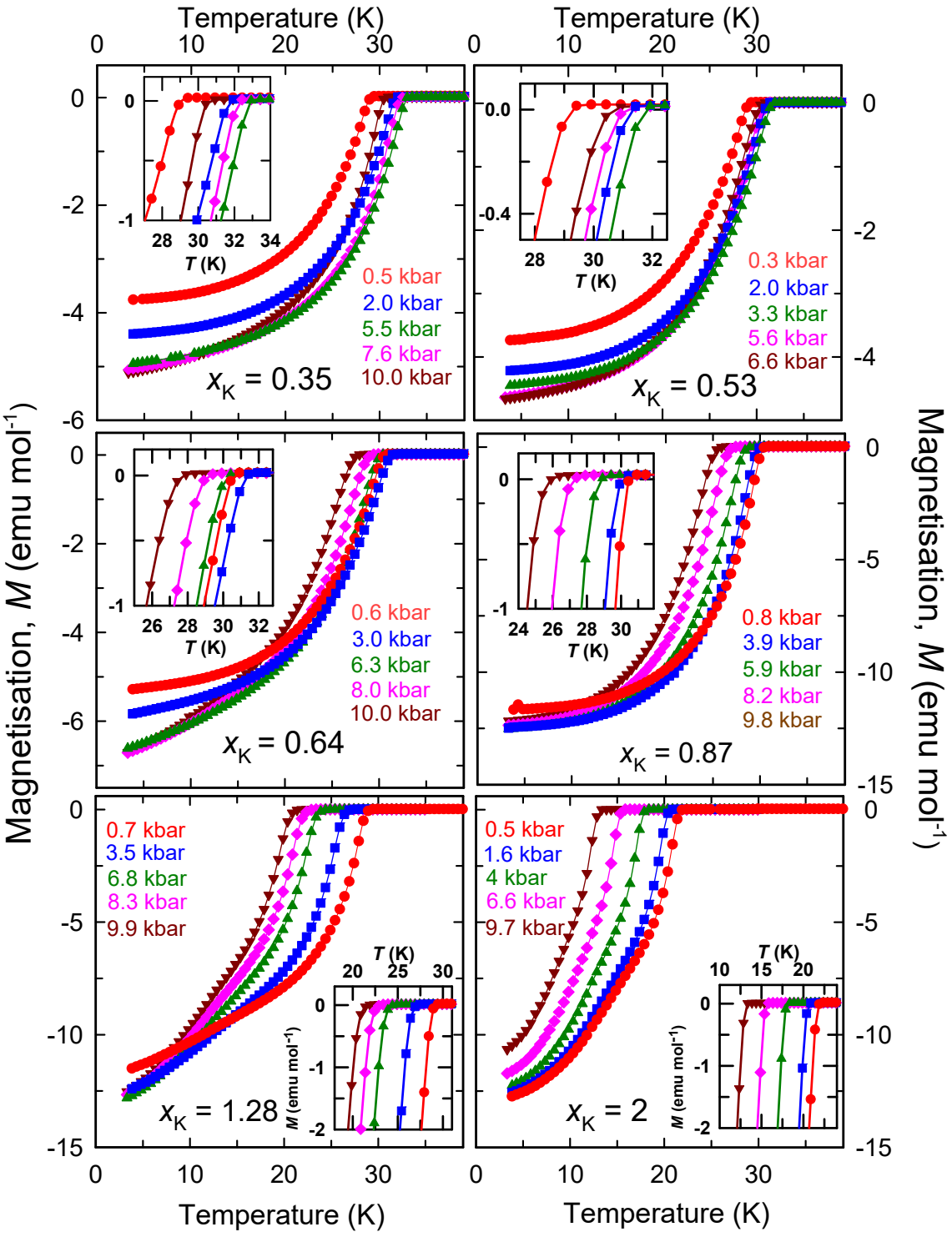

Fig. S22 Temperature dependence of the ZFC magnetisation, M, divided by the applied magnetic field (20 Oe) at selected pressures for the $K_xCs_{3-x}C_{60}$ samples. The insets show expanded regions of the respective $M(T)$ data near the superconducting T_c.

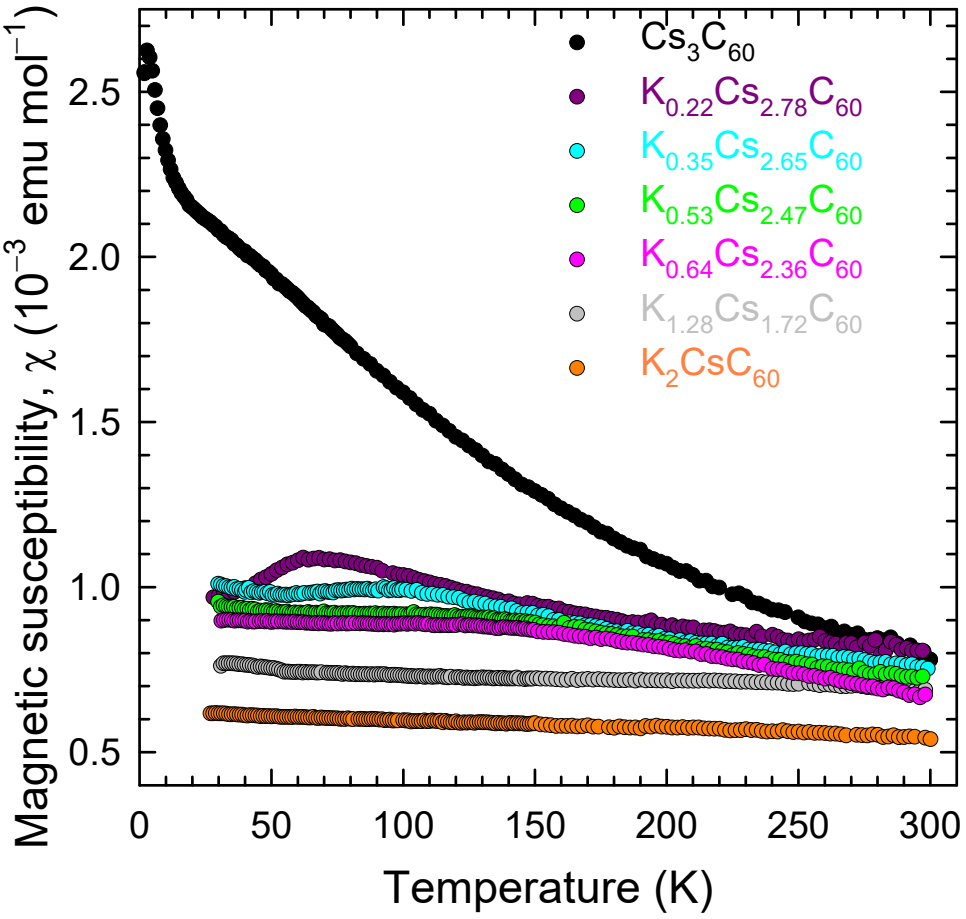

Fig. S23 Temperature dependence of the magnetic susceptibility, $\chi(T)$, of the $K_xCs_{3-x}C_{60}$ ($0 \le x \le 2$) phase assemblages. The data for fcc-structured Cs_3C_{60} are taken from ref. [7].

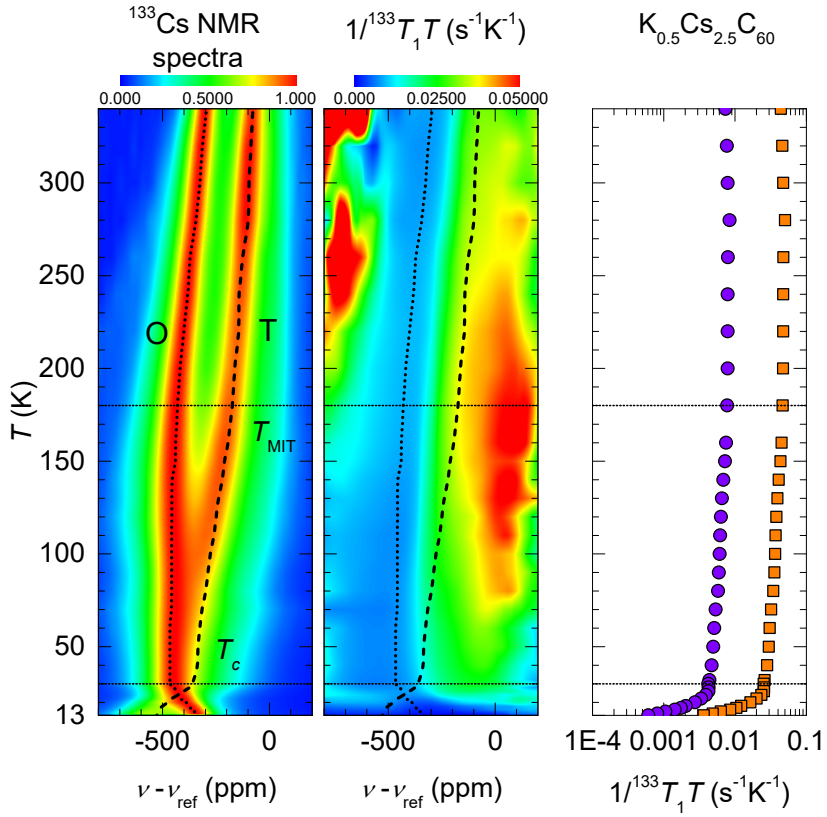

Fig. S24 (*Left panel*) Evolution of the normalised ^{133}Cs NMR spectral intensity of $K_{0.64}Cs_{2.36}C_{60}$ with temperature shows significant overlap between the O and T peaks below ~100 K. Dotted and dashed lines mark the temperature variation of the centre of gravity of the O and T components, respectively. (*Middle panel*) Plot of ^{133}Cs spin-lattice relaxation rate divided by temperature, $1/^{133}T_1T$, extracted at various points of the ^{133}Cs NMR spectra as a function of temperature demonstrates that $1/^{133}T_1$ for the O site is by a factor of 6(1) smaller than that for the more tightly packed T sites. Red-coloured patches are analysis artefacts in parts where the ^{133}Cs NMR spectral intensity is extremely small. (*Right panel*) Temperature dependence of $1/^{133}T_1T$ for O (purple circles) and T (orange squares) peaks when the ratio between $1/^{133}T_1$ for the T and O sites is fixed to 6. In all panels, horizontal thin dotted lines mark the metal-insulator crossover temperature, T^* = 170 K and zero-field superconducting critical temperature, T_c = 30.5 K.

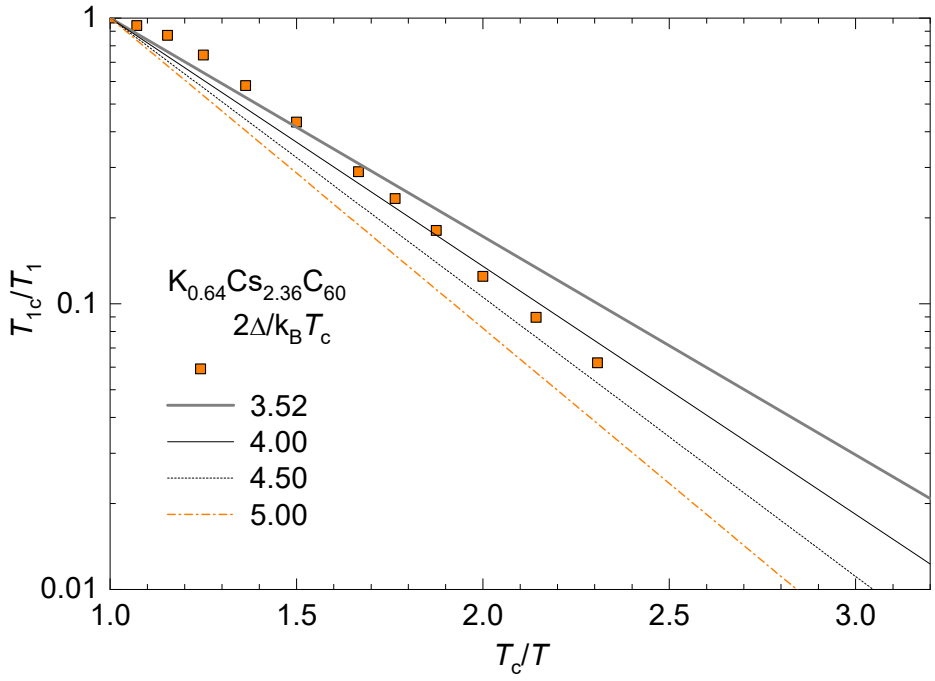

Fig. S25 ^{133}Cs spin-lattice relaxation rate, $1/^{133}T_1$ normalized to its value at T_c *vs* inverse temperature, T_c/T for $K_{0.64}Cs_{2.36}C_{60}$ (orange squares). Lines show the expected slopes of $1/^{133}T_1 \propto \exp[-\Delta_0/k_BT]$ calculated for $2\Delta_0/k_BT_c$ of 3.52 (thick solid line), 4 (dashed line), 4.5 (dotted line) and 5 (orange dash-dot line). The slope of data for $(T_c/T) > 1.25$ matches $2\Delta_0/k_BT_c = 5$.

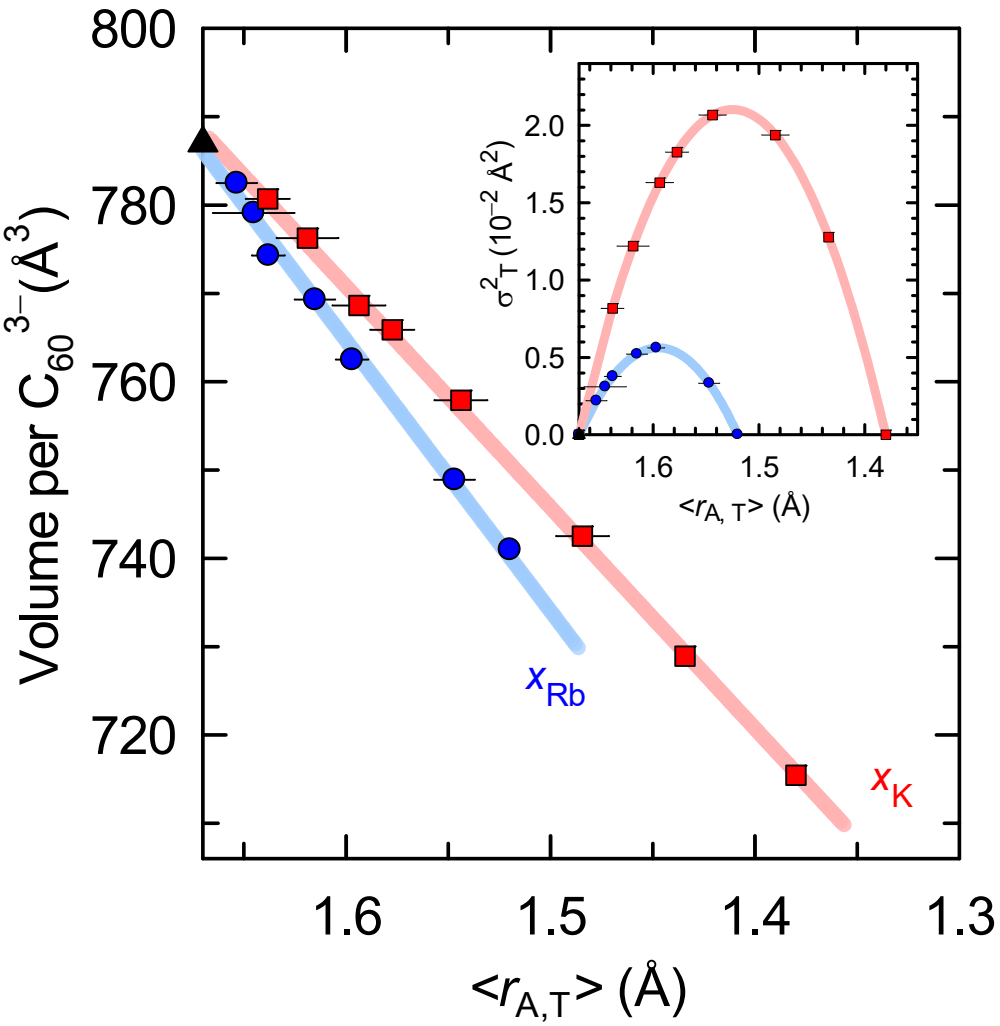

Fig. S26 Variation of the packing density, V per C_{60}^{3-} at $T = T_c$ with average ionic radius of the ions in the tetrahedral interstices, $\langle r_{A,T}\rangle$ for the $K_{3-x}Cs_xC_{60}$ (red) and $Rb_{3-x}Cs_xC_{60}$ (blue) compositions. Solid lines through the data points are linear fits to the data yielding $dV/d\langle r_{A,T}\rangle$ = 250(3) and 306(9) Å^2 for A = K (red squares) and Rb (blue circles [6]), respectively. The black triangle is the datum for Cs_3C_{60} [7]. The *inset* shows the variation of cation disorder at the T-site, σ_T^2 with the average size of the T-site cation radius, $\langle r_{A,T}\rangle$.